

The Great Observatories All-Sky LIRG Survey: Comparison of Ultraviolet and Far-Infrared Properties

Justin H. Howell,¹ Lee Armus,¹ Joseph M. Mazzarella,² Aaron S. Evans,^{3,4} Jason A. Surace,¹ David B. Sanders,⁵ Andreea Petric,¹ Phil Appleton,⁶ Greg Bothun,⁷ Carrie Bridge,^{1,11} Ben H.P. Chan,² Vassilis Charmandaris,^{8,9} David T. Frayer,⁶ Sebastian Haan,¹ Hanae Inami,¹ Dong-Chan Kim,³ Steven Lord,⁶ Barry F. Madore,^{2,10} Jason Melbourne,¹¹ Bernhard Schulz,⁶ Vivian U,⁵ Tatjana Vavilkin,¹² Sylvain Veilleux,¹³ Kevin Xu⁶

ABSTRACT

The Great Observatories All-sky LIRG Survey (GOALS) consists of a complete sample of 202 Luminous Infrared Galaxies (LIRGs) selected from the IRAS Revised Bright Galaxy Sample (RBGS). The galaxies span the full range of interaction stages, from isolated galaxies to interacting pairs to late stage mergers. We present a comparison of the UV and infrared properties of 135 galaxies in GOALS observed by GALEX and Spitzer. For interacting galaxies with separations greater than the resolution of GALEX and Spitzer ($\sim 2 - 6''$), we assess the UV and IR properties of each galaxy individually. The contribution of the FUV to the measured SFR ranges from 0.2% to 17.9%, with a median of 2.8% and a mean of $4.0 \pm 0.4\%$. The specific star formation rate of the

¹Spitzer Science Center, MS 220-6, California Institute of Technology, Pasadena, CA 91125; jhhowell@ipac.caltech.edu

²Infrared Processing & Analysis Center, MS 100-22, California Institute of Technology, Pasadena, CA 91125

³Department of Astronomy, University of Virginia, P.O. Box 400325, Charlottesville, VA 22904

⁴National Radio Astronomy Observatory, 520 Edgemont Road, Charlottesville, VA 22903

⁵Institute for Astronomy, University of Hawaii, 2680 Woodlawn Drive, Honolulu, HI 96822

⁶NASA Herschel Science Center, IPAC, MS 100-22, California Institute of Technology, Pasadena, CA 91125

⁷Department of Physics, University of Oregon, Eugene, OR 97403

⁸University of Crete, Department of Physics, Heraklion 71003, Greece

⁹IESL/Foundation for Research and Technology - Hellas, GR-71110, Heraklion, Greece and Chercheur Associé, Observatoire de Paris, F-75014, Paris, France

¹⁰The Observatories, Carnegie Institution of Washington, 813 Santa Barbara Street, Pasadena, CA 91101

¹¹Caltech Optical Observatories, Division of Physics, Mathematics and Astronomy, Mail Stop 320-47, California Institute of Technology, Pasadena, CA 91125

¹²Department of Physics and Astronomy, State University of New York at Stony Brook, Stony Brook, NY 11794-3800

¹³Department of Astronomy, University of Maryland, College Park, MD 20742

GOALS sample is extremely high, with a median value ($3.9 \times 10^{-10} \text{ yr}^{-1}$) that is comparable to the highest specific star formation rates seen in the Spitzer Infrared Nearby Galaxies Survey sample. We examine the position of each galaxy on the IR excess–UV slope (IRX- β) diagram as a function of galaxy properties, including IR luminosity and interaction stage. The LIRGs on average have greater IR excesses than would be expected based on their UV colors if they obeyed the same relations as starbursts with $L_{IR} < 10^{11} L_{\odot}$ or normal late-type galaxies. The ratio of L_{IR} to the value one would estimate from the IRX- β relation published for lower luminosity starburst galaxies ranges from 0.2 to 68, with a median value of 2.7. A minimum of 19% of the total IR luminosity in the RBGS is produced in LIRGs and ULIRGs with red UV colors ($\beta > 0$). Among resolved interacting systems, 32% contain one galaxy which dominates the IR emission while the companion dominates the UV emission. Only 21% of the resolved systems contain a single galaxy which dominates both wavelengths.

Subject headings: ultraviolet: galaxies, infrared: galaxies

1. Introduction

The Infrared Astronomical Satellite (IRAS) provided the first unbiased survey of the sky at mid and far-infrared wavelengths, giving us a comprehensive census of the infrared emission properties of galaxies in the local Universe. A major result of this survey was the discovery of a large population of luminous infrared galaxies (LIRGs) which emit a large majority of their bolometric luminosity in the far-infrared, and have $10^{11} \leq L_{IR}[8 - 1000\mu\text{m}] < 10^{12} L_{\odot}$. LIRGs are a mixture of single galaxies, disk galaxy pairs, interacting systems, and advanced mergers. They exhibit enhanced star-formation rates and a higher fraction of Active Galactic Nuclei (AGN) compared to less luminous and non-interacting galaxies (Sanders & Mirabel 1996 and references therein). At the highest luminosities, ultraluminous infrared galaxies (ULIRGs: $L_{IR} \geq 10^{12} L_{\odot}$) may represent an important evolutionary stage in the formation of QSOs (Sanders et al. 1988a,b) and massive ellipticals (e.g., Genzel et al. 2001; Tacconi et al. 2002). Since LIRGs comprise the bulk of the cosmic infrared background and dominate the star-formation activity between $0.5 < z < 1$ (Le Floc'h et al. 2005; Caputi et al. 2006), they may also play a key role in our understanding of the general evolution of galaxies and black holes (e.g., Magorrian et al. 1998).

The Great Observatories All-sky LIRG Survey (GOALS; Armus et al. 2009) contains a complete sample of low-redshift LIRGs and ULIRGs with observations across the electromagnetic spectrum. The GOALS targets are drawn from the IRAS Revised Bright Galaxy Sample (RBGS; Sanders et al. 2003), a complete sample of 629 galaxies with IRAS 60 μm flux densities $S_{60} > 5.24 \text{ Jy}$, covering the full sky above Galactic latitudes $|b| > 5$ degrees. The 629 galaxies have a median redshift of $z = 0.008$ and a maximum redshift of $z = 0.088$. There are 181 LIRGs and 21 ULIRGs in the RBGS, and these galaxies define the GOALS sample.

In LIRGs and ULIRGs, UV radiation is produced by young stars and AGN. A fraction of the UV radiation is absorbed by dust and re-radiated in the far-infrared. To understand the power sources in these galaxies, it is essential to fully characterize the energy budget by measuring both the emerging UV and the infrared flux. The relationship between the UV continuum slope and the infrared excess (the IRX- β correlation) provides a useful parameterization of this energy budget. Charlot & Fall (2000) showed that the IRX- β relation is a sequence in effective optical depth for star forming systems. However this relation does not hold in all systems. While lower luminosity starbursts follow the correlation, ULIRGs do not (Meurer, Heckman, & Calzetti 1999; Goldader et al. 2002). The GOALS sample allows us to explore the IRX- β correlation precisely over the luminosity range where it breaks down. A detailed study of LIRGs may indicate the luminosity threshold or the time during the merger when the UV slope becomes decoupled from the IR emission. Being a flux limited sample of the nearest and most well studied LIRGs and ULIRGs, GOALS provides an important local benchmark against which to compare the observed visual properties of high redshift galaxies. This paper looks at global UV and IR properties. Future work will address nearby spatially resolved LIRGs.

This paper is divided into five sections. The data are discussed in § 2. Analysis of the sample is presented in § 3, results are discussed in § 4, and conclusions are given in § 5. A cosmology of $\Omega_{\Lambda} = 0.72$, $\Omega_m = 0.28$, with $H_0 = 70 \text{ km s}^{-1} \text{ Mpc}^{-1}$ is adopted throughout.

2. Observations and Data Reduction

The GOALS GALEX sample consists of 135 systems observed as part of GALEX Cycle 1 program #13 (PI Mazzarella), GALEX Cycle 5 program #38 (PI Howell), the Nearby Galaxy Survey (NGS), and the All Sky Survey (AIS). All systems have been observed in both the FUV ($\lambda_{\text{eff}} = 1528\text{\AA}$) and NUV ($\lambda_{\text{eff}} = 2271\text{\AA}$). Integration times range from $\sim 100\text{s}$ for the AIS data to $> 1500\text{s}$ for the Cycle 1, Cycle 5, and NGS data. Aside from a handful of galaxies not yet observed from the Cycle 5 program, the 135 systems described here represent all GOALS targets accessible to GALEX.

Photometry was performed on the standard GALEX pipeline data products. Since GALEX backgrounds are very low, especially for FUV images, standard photometry codes often return a background value of zero. To accurately measure the background in these images, we followed the prescription of Gil de Paz et al. (2007, hereafter GDP) using software written by those authors and made available to us. Standard IDL aperture photometry codes were used to measure the total UV fluxes inside large apertures (typically $1'$ radius) matched to Spitzer $24 \mu\text{m}$ MIPS photometry (Mazzarella et al. 2010). Aperture centers were taken from Armus et al. (2009). The resultant UV GALEX photometry of the sample is presented in Table 1. In the case of widely separated pairs, only the more IR-luminous component is listed. Close pairs are treated as a single system, with the combined flux density listed in the table.

To test the accuracy of our measurements and to ensure meaningful comparisons with published data sets such as GDP, galaxies with D25 ellipses (de Vaucouleurs et al. 1991) were measured in D25 elliptical apertures. Little difference was found between the fluxes measured in the D25 aperture as compared to the circular aperture. The seven targets in common with the sample of GDP revealed a systematic shift in the photometric calibration between different versions of the GALEX data reduction pipeline. To account for this, the GDP fluxes have been adjusted for purposes of comparison with the GOALS sample. The raw count rates (before background subtraction) have been multiplied by factors of 0.89 (FUV) and 1.05 (NUV). Fluxes and magnitudes were then recalculated after background subtraction.

The resolution of Spitzer allows many interacting pairs or groups to be resolved into their component galaxies in the IR. For systems with separations greater than $0.5'$, the $70\ \mu\text{m}$ flux ratio was used to estimate the fraction of the IRAS L_{IR} coming from each galaxy. Similarly, the $24\ \mu\text{m}$ flux ratio was used for systems separated by $0.12' < d < 0.5'$, and systems which saturated at $70\ \mu\text{m}$. The latter method is inaccurate for systems in which the two galaxies have different far-IR colors, such as the Arp 299 (NGC3690/IC0694) system (see Charmandaris, Stacey, & Gull 2002). A total of 93 galaxies in 44 GOALS systems have been resolved in one or both GALEX FUV and NUV images. Photometry of the resolved sources is presented in Table 2.

3. Results

3.1. UV Luminosities and Spectral Slopes

Although selected to be IR luminous, the GOALS sample spans a wide range of UV luminosities. The FUV flux densities range from 2.4×10^{-16} to 2.9×10^{-13} $\text{erg s}^{-1}\text{cm}^{-2}\text{\AA}^{-1}$, with a median of 7.3×10^{-15} $\text{erg s}^{-1}\text{cm}^{-2}\text{\AA}^{-1}$ and a mean of $(1.7 \pm 0.4) \times 10^{-14}$ $\text{erg s}^{-1}\text{cm}^{-2}\text{\AA}^{-1}$. The NUV flux densities range from 6.8×10^{-16} to 2.6×10^{-13} $\text{erg s}^{-1}\text{cm}^{-2}\text{\AA}^{-1}$ with a median of 5.1×10^{-15} $\text{erg s}^{-1}\text{cm}^{-2}\text{\AA}^{-1}$ and a mean of $(1.3 \pm 0.3) \times 10^{-14}$ $\text{erg s}^{-1}\text{cm}^{-2}\text{\AA}^{-1}$. The log of the FUV luminosities range from 8.30 to 10.33, with a median and a mean of 9.45 ± 0.04 , where the luminosities are expressed in solar units, uncorrected for reddening. The log of the NUV luminosities range from 8.30 to 10.40, with a median of 9.57 and a mean of 9.64 ± 0.04 . For comparison, the characteristic luminosity L_* for the present day FUV luminosity function is $10^{9.6} L_\odot$ (Wyder et al. 2005). The GOALS sample is thus on average only 30% fainter than L_* in the FUV, and the most UV-luminous LIRGs in GOALS are ultraviolet luminous galaxies (UVLGs, defined as $\log(L_{\text{FUV}}/L_\odot) > 10.3$; Heckman et al. 2005).

The infrared excess IRX is defined as the ratio of IR to FUV flux, most commonly expressed in logarithmic units. When calculating IRX we use L_{IR} , the total IR luminosity from 8–1000 μm . L_{IR} is calculated using IRAS flux densities for integrated systems, and is allocated among resolved galaxies using MIPS flux density ratios as described above. IRAS flux densities for GOALS systems are taken from Sanders et al. (2003), MIPS flux densities for resolved galaxies within GOALS sys-

tems are taken from Mazzarella et al. (2010), and luminosity distances are taken from Armus et al. (2009). IRX values range from 1.08 to 3.42, with a median of 2.02 and a mean of 2.06 ± 0.04 . Derived quantities are presented in Table 3 for integrated systems and in Table 4 for resolved galaxies.

The UV continuum slope $\beta(\text{GALEX})$ was calculated according to the definition of Kong et al. (2004):

$$\beta(\text{GALEX}) = \frac{\log(f_{\text{FUV}}) - \log(f_{\text{NUV}})}{-0.182} \quad (1)$$

where f_{FUV} and f_{NUV} are the mean flux densities per unit wavelength. Values of $\beta(\text{GALEX})$ range from -1.28 to 3.5, with a median of -0.16 and a mean of 0.07 ± 0.08 . Since the GALEX filters have different effective wavelengths than previous instruments such as IUE or STIS, the normalization of $\beta(\text{GALEX})$ is different from previous work (e.g., Meurer et al. 1999; Goldader et al. 2002; see Appendix A for a more detailed discussion and a direct conversion between $\beta(\text{GALEX})$ and $\beta(\text{IUE})$). Of the 135 observed systems, 112 have good quality data ($\sigma_{\beta(\text{GALEX})} < 0.5$) and are used in the subsequent analysis. Eleven galaxies in the Meurer et al. (1999) sample are included in GDP. These systems allow us to recreate the linear portion of the IRX- $\beta(\text{GALEX})$ relation for (sub-LIRG) starburst galaxies, hereafter referred to as the starburst relation. The eleven Meurer et al. (1999) systems in GDP span a range of $-1 < \beta(\text{GALEX}) < 0.5$, and extrapolations beyond that range are not necessarily correct.

The IRX- $\beta(\text{GALEX})$ plot is shown in Fig. 1. As Goldader et al. (2002) discovered, IR-luminous systems tend to lie above the starburst relation. Similarly, as seen in Kong et al. (2004), Cortese et al. (2006), and GDP, the starburst relation forms an upper envelope for normal galaxies on this plot. Within the valid range for the starburst relation, 15% of LIRGs fall below the relation. In addition, twelve LIRGs with very red UV colors ($\beta > 1$) have high IRX values (2.2–3.3) but lie far below a linear extrapolation to the starburst relation. The fit to the late-type galaxy sample of Cortese et al. (2006) provides a particularly clean separation between (U)LIRGs and sub-LIRGs in Fig. 1. The shallower slope better matches the distributions of GOALS subpopulations ($L_{\text{IR}} < 10^{11.4}$, $10^{11.4} < L_{\text{IR}} < 10^{11.8}$, and $L_{\text{IR}} > 10^{11.8}$), with the more luminous subpopulations having larger separations in IRX from the Cortese relation. The best fit slope for the GOALS data is $\text{IRX} = (0.46 \pm 0.06)\beta + (2.1 \pm 0.1)$, shallower than the Cortese relation by 0.24 but offset to higher IRX by 0.8 at $\beta = 0$.

3.2. Star Formation Rates

The combination of IRAS L_{IR} and GALEX FUV measurements provide an estimate of the total (obscured plus unobscured) star formation rate (SFR; Kennicutt 1998; Dale et al. 2007). The contribution of the FUV to the measured SFR ranges from 0.2% to 17.9%, with a median of 2.8% and a mean of $4.0 \pm 0.4\%$. A histogram showing the ratio of UV-derived SFR to that derived from the combination of UV and IR luminosity is shown in Fig. 2a. Calculations relating to SFR

do not include galaxies with IRAC colors that are consistent with the presence of a strong AGN (Stern et al. 2005). The distribution of the FUV contribution to SFR is consistent with previous work (Surace & Sanders 2000; Surace, Sanders, & Evans 2000). The FUV contribution to SFR is small for LIRGs and ULIRGs, and decreases as L_{IR} increases (Fig. 2b). The Spearman rank correlation coefficient $r_s = -0.47$, with significance 3.6×10^{-6} indicating a significant correlation, although the relation is clearly non-linear. Galaxies with larger infrared luminosity have a higher fraction of their measured star-formation emerging in the far-infrared, with a corresponding lower fraction emerging in the far-ultraviolet. As a function of IR luminosity, the median (mean) contribution of the FUV to the measured SFR is 3.3% (4.6%) for systems with $L_{IR} < 10^{11.8}$, and drops to 1.9% (2.0%) for systems with $L_{IR} > 10^{11.8}$.

IRAC 3.6 μm and 2MASS K band photometry were used to estimate the stellar mass of each galaxy (Lacey et al. 2008). The mass estimates derived from K band data were used where possible. For the galaxies without reliable K-band photometry, the masses estimated from 3.6 μm data were scaled by the median ratio of mass(K)/mass(3.6) from galaxies measured at both wavelengths. Stellar masses range from 4.3×10^{10} to $6.4 \times 10^{11} M_\odot$, with a median of $1.4 \times 10^{11} M_\odot$ and a mean of $(1.63 \pm 0.09) \times 10^{11} M_\odot$. The specific star formation rate (SFR per unit mass; SSFR) ranges from 5.5×10^{-11} to $3.5 \times 10^{-9} \text{ yr}^{-1}$, with a median of $3.9 \times 10^{-10} \text{ yr}^{-1}$ and a mean of $(6.2 \pm 0.7) \times 10^{-10} \text{ yr}^{-1}$. These correspond to mass doubling timescales of 18 Gyr to 290 Myr, with a median of 2.6 Gyr.

The Spitzer Infrared Nearby Galaxy Survey (SINGS; Kennicutt et al. 2003) provides a useful comparison sample of lower luminosity galaxies observed with both GALEX and Spitzer. The upper bound of the SSFRs measured for SINGS galaxies is approximately $3 \times 10^{-10} \text{ yr}^{-1}$ (Dale et al. 2007). The IR/UV ratio, a useful observational measure of dust extinction, is defined as

$$\text{IR/UV} = \frac{L_{IR}}{\nu L_\nu(\text{FUV}) + \nu L_\nu(\text{NUV})} \quad (2)$$

and ranges from 5.8 to 813, with a median of 39. Figure 3 compares the IR/UV ratio against SSFR for both the GOALS and SINGS samples (Dale et al. 2007). In GOALS systems, the IR/UV ratio is correlated with SSFR ($r_s = 0.55$, significance 2×10^{-8}), with large scatter: LIRGs and ULIRGs with high SSFR also have high IR/UV ratios. The two quantities are anti-correlated ($r_s = -0.61$, significance 1×10^{-6}) for SINGS galaxies with $\text{SSFR} > 10^{-11} \text{ yr}^{-1}$. A handful of SINGS galaxies have IR/UV ratios which are as high as seen in the GOALS sample, but their SSFRs are significantly lower. Taken together, the GOALS and SINGS sources span nearly four orders of magnitude in IR/UV at high SSFR ($> 10^{-10} \text{ yr}^{-1}$), probing very different star forming populations.

To investigate subpopulations of the GOALS sample in SSFR, we define bins with $\text{SSFR} < 3 \times 10^{-10} \text{ yr}^{-1}$, $3 \times 10^{-10} < \text{SSFR} < 6 \times 10^{-10} \text{ yr}^{-1}$, and $\text{SSFR} > 6 \times 10^{-10} \text{ yr}^{-1}$: galaxies which span the same range of SSFR as the SINGS sample, galaxies with up to twice the SSFR as the most extreme SINGS galaxies, and galaxies with more than twice the SSFR of the most extreme SINGS galaxies, respectively. These subpopulations are plotted on the IRX- β (GALEX) diagram in Fig. 4.

The systems with higher SSFR have higher median offsets from the starburst relation than systems with lower SSFR. Median β values are -0.2 ± 0.2 , 0.1 ± 0.1 , and -0.20 ± 0.09 (high, medium, and low SSFR bins, respectively). Median IRX values are 2.35 ± 0.09 , 2.10 ± 0.08 , and 1.81 ± 0.06 , respectively. Systems with $\beta < 0.5$ allowing a direct comparison to the starburst relation have median vertical deviations of 0.9 ± 0.1 , 0.4 ± 0.1 , and 0.37 ± 0.09 respectively.

3.3. Resolved Systems

A number of the interacting LIRGs in GOALS are near enough to resolve with both GALEX and Spitzer and derive IR and UV properties for each galaxy. Derived quantities for the galaxies in resolved systems are presented in Table 4. The component galaxies of resolved pair/triple systems are plotted on the IRX- β (GALEX) diagram in Fig. 5. Many GOALS systems consist of a LIRG with one or more sub-LIRG companions. The sub-LIRG galaxies are on average consistent with the GDP sample. LIRGs are on average offset above the starburst relation, with $L_{IR} > 10^{11.4}L_{\odot}$ systems having larger offsets than lower luminosity LIRGs. For systems with $\beta < 0.5$, median offsets are 1.1 ± 0.2 and 0.4 ± 0.1 for the $L_{IR} > 10^{11.4}L_{\odot}$ and $10^{11} < L_{IR} < 10^{11.4}L_{\odot}$ populations, respectively. An individual galaxy in general does not lie in the same region of the IRX- β diagram as the LIRG system of which it is a component; see §4.3 for further discussion.

Of the 18 resolved systems for which masses could be estimated, the median mass ratio of the galaxy companions is 2.6:1, with a range from 1.1:1 to 8.1:1. The high mass component of these pairs/triples is, on average, offset above the starburst relation (Fig. 6), while the low mass components are, on average, consistent with the starburst relation. For systems with $\beta < 0.5$, median offsets are 0.9 ± 0.1 and 0.3 ± 0.1 for the high mass and low mass components, respectively.

4. Discussion

The complete sample of the nearest LIRGs and ULIRGs that comprise GOALS is ideal for studying the relationship between the IR and UV properties of luminous infrared galaxies. A key diagnostic tool which we explore in this paper is the IRX- β (GALEX) diagram, comparing the IR excess (ratio of IR to FUV emission) to the FUV-NUV color parameterized as the power-law slope β (GALEX). If a class of galaxies, such as starburst galaxies, follows tight relations on this diagram, then the measurement of the rest-frame UV color allows IRX and thus L_{IR} to be derived. This is of particular interest at high redshift, where L_{IR} can only be directly measured using far-infrared and submillimeter observations but rest-frame UV observations can be made at visual wavelengths in deep surveys. Since LIRGs contribute significantly to the star-formation activity at high redshift (e.g., Magnelli et al. 2009), understanding the IRX- β (GALEX) relation in this population is extremely important. The IRX- β (GALEX) diagram, and the combination of UV and IR data more generally, provide an indication of the obscuration to the young stars (or active

nucleus) within a galaxy. This can provide a rough test of the evolutionary sequence in which some starburst galaxies transition from LIRGs to ULIRGs to QSO hosts over the course of a major merger event as the dust and gas is first funneled towards the nuclei fueling a starburst, only to be cleared away by the action of AGN and starburst winds in the final stages of the transformation to a QSO.

To estimate the importance of high- β galaxies among the IR population as a whole, the fraction of the total IR luminosity integrated over all 629 galaxies in the RBGS contributed by the 112 LIRGs and ULIRGs of the GOALS GALEX sample is shown as a function of β in Fig. 7. Within the GOALS sample, more luminous systems have, on average, larger IRX and redder β values than less luminous systems while maintaining roughly the same offset from the starburst relation. As shown in Fig. 7, a minimum of 19% of the total infrared luminosity of the 629 galaxies that comprise the RBGS is produced in LIRGs and ULIRGs with a $\beta > 0$ (IUE or GALEX). These red sources are typically absent from UV-selected samples at high redshift, regardless of their estimated IR luminosity. This is a strict lower limit, since there are a number of low- z LIRGs not observed or detected with GALEX which might have large β .

4.1. Explaining Scatter in the IRX- β (GALEX) Relation

The trend for certain populations to have, on average, larger values of IRX and redder values of β (GALEX) (parallel to the starburst relation) has been explained as a sequence in optical depth (Charlot & Fall 2000). Thus, on average, more luminous LIRGs and ULIRGs have more extinction than less luminous LIRGs, and interacting systems have more extinction than non-interacting systems. This is consistent with the evolutionary scenario mentioned earlier.

We interpret the scatter of LIRGs and ULIRGs in the IRX- β (GALEX) diagram as follows. Deviations to the right of the starburst relation are interpreted as purely the result of redder UV colors (extra NUV emission for a given amount of FUV emission), most likely due to light from older stellar populations (Kong et al. 2004). Deviations above the starburst relation are interpreted as the result of increases in IRX, which we define as Δ IRX. This quantity is a measure of the extent to which the IR and UV emission become decoupled, for example in heavily obscured nuclei which emit strongly in the FIR (UV radiation reprocessed by dust) but do not contribute to the observed (escaping) UV emission. Like the starburst relation, Δ IRX is not necessarily accurate for β (GALEX) < -1 or β (GALEX) > 0.5 . A minimum of 11% of the total L_{IR} of the RBGS sample is produced in LIRGs and ULIRGs with Δ IRX > 1 , an order of magnitude above the starburst relation.

Cortese et al. (2006) concluded that attempting to estimate L_{IR} from rest-frame UV data of high redshift galaxies will be uncertain by $> 50\%$ for normal galaxies. We find that using the starburst relation to estimate L_{IR} from rest-frame UV observations of LIRGs and ULIRGs would on average underestimate L_{IR} by a factor of 2.7 with a range of $L_{IR}(\text{true})/L_{IR}(\text{estimated})$ between

0.2 to 68. Overestimates can be much greater for red UV colors beyond the range of the starburst relation ($\beta(\text{GALEX}) > 0.5$), up to a factor of 2400 for a linear extrapolation. Previous studies have investigated possible second parameters for the scatter of normal galaxies to the right the starburst relation. Using a sample of a wide variety of galaxy types, Seibert et al. (2005) found no correlation between the deviation from the starburst relation and L_{IR} , L_{UV} , L_{bol} , or UV and optical colors. Among normal galaxies, any correlation with star formation history is weak (Kong et al. 2004; Cortese et al. 2006) or nonexistent (Seibert et al. 2005; Boquien et al. 2009).

A number of observables might explain the scatter in ΔIRX , providing a second parameter to allow more accurate measurements of L_{IR} at high redshift as well as physical insight into the evolution of LIRGs and ULIRGs. A central question is what mechanism(s) lead to the UV emission being heavily obscured or decoupled from the IR emission in (U)LIRGs (Goldader et al. 2002) but not in lower luminosity starbursts? Since many LIRGs and essentially all ULIRGs are merger remnants with intense, compact, dust-enshrouded nuclear starbursts or AGN, a concentration parameter might correlate with $\text{IRX}-\beta(\text{GALEX})$ scatter as an indicator of decoupled IR and UV emission. Similarly, warm IR colors such as IRAS 25 $\mu\text{m}/60 \mu\text{m}$ might indicate dust in close proximity to a powerful UV source (starburst or AGN). AGN provide another possible mechanism to explain scatter from the starburst relation. The [3.6]-[4.5] and [5.8]-[8] IRAC colors (Stern et al. 2005) can be used as an indicator of AGN emission. Systems identified as potential AGN might correlate with larger IRX above what the starburst relation would predict. Finally, although heightened IRX in a population of LIRGs and ULIRGs is most logically explained by elevated IR emission, it is possible for low UV emission to produce the same result.

As shown in Fig. 8, ΔIRX increases with IR luminosity for $L_{IR} \gtrsim 10^{10} L_{\odot}$, with considerable scatter. GOALS systems with IRAC colors that may indicate the presence of an AGN tend to have larger IRX ratios by a factor of six. No correlation is found between ΔIRX and any of the following quantities: IRAS 25 $\mu\text{m}/60 \mu\text{m}$ color, IRAS 60 $\mu\text{m}/100 \mu\text{m}$ color, Spitzer 8 $\mu\text{m}/24 \mu\text{m}$ color, L_{FUV} , 8 μm concentration (1 kpc/Total). The lack of correlation between ΔIRX and global parameters other than L_{IR} suggest that the decoupling between UV and IR emission takes place on sub-kpc scales in most LIRGs and ULIRGs, well below our resolution with GALEX and Spitzer MIPS 24 μm , which is 2.6 kpc ($6''$) at the median distance of the GOALS sample (89 Mpc). Future studies (e.g. with Herschel and HST) at higher spatial resolution in the FIR and UV will be able to investigate this further. Such studies have already been done for a few nearby quiescent star-forming galaxies. Boquien et al. (2009) found that variation in dust extinction curves and geometry is the most important factor determining the location of individual star-forming regions on the $\text{IRX}-\beta$ diagram. Muñoz-Mateos et al. (2009) examined radial profiles of all available SINGS galaxies and found that star formation history is the primary driver determining the position on the $\text{IRX}-\beta$ diagram of a radial annulus within a galaxy. The lack of correlation between ΔIRX and FIR colors suggests that when dust is close to the heating source (producing warm FIR colors), that source is obscured and the UV color $\beta(\text{GALEX})$ increases along with IRX. Galaxies with positive ΔIRX span a range of $\log(L_{FUV})$ from 8.6 to 10.3 uniformly. The range of FUV luminosities indicates

that LIRGs and ULIRGs with large ΔIRX value are IR-bright, not UV-faint. Figure 9 shows the IR/UV ratio and ΔIRX plotted against the 1600Å luminosity (derived by linear interpolation between FUV and NUV).

In order to explore the dependence of IRX and β on the morphological properties of LIRGs, all GOALS systems were visually classified as either interacting or non-interacting based on the inspection of the Spitzer IRAC 3.6um images. A galaxy was deemed interacting if it exhibited a tidal bridge or tail, double nuclei, multiple galaxies in a common envelope or a disturbed morphology. The interacting and non-interacting subpopulations are shown on the IRX- β (GALEX) diagram in Fig. 10. Although the median position of the interacting population has redder β (median 0.0 vs. -0.19) and larger IRX (2.01 vs. 1.86) than the non-interacting population, the two populations are consistent with being drawn from the same distribution. The galaxies with the lowest IRX are predominantly interacting, and these systems are among the most UV-luminous sources in the GOALS sample with $\log(L_{\text{FUV}}/L_{\odot}) \gtrsim 10$.

UVLGs are an interesting type of object to compare with (U)LIRGs since they are objects with extremely high SFR but little dust obscuration. Five LIRGs in our sample are also UVLGs or near-UVLGs ($L_{\text{FUV}} \geq 10^{10.2}L_{\odot}$): Arp 256, VV 114, Arp 240, NGC 6090, and CGCG 448-020. The stellar masses of these systems range from $11.1 \leq \log(M_{\text{stellar}}/M_{\odot}) \leq 11.5$. SFR derived from the combination of UV and IR luminosities range from $1.8 \leq \log(\frac{\text{SFR}}{M_{\odot}\text{yr}^{-1}}) \leq 2.2$, and SSFR range from $-9.6 \leq \log(\text{SSFR}/\text{yr}^{-1}) \leq -8.9$. The sample of Heckman et al. (2005) is divided into Large UVLGs and Compact UVLGs, which have mass ranges of $10.5 \leq \log(M_{\text{stellar}}/M_{\odot}) \leq 11.1$ and $9.5 \leq \log(M_{\text{stellar}}/M_{\odot}) \leq 10.7$ respectively, SFR ranges of $0.6 \leq \log(\frac{\text{SFR}}{M_{\odot}\text{yr}^{-1}}) \leq 1.2$ and $0.6 \leq \log(\frac{\text{SFR}}{M_{\odot}\text{yr}^{-1}}) \leq 1.4$ respectively, and SSFR ranges of $-10.5 \leq \log(\text{SSFR}/\text{yr}^{-1}) \leq -9.5$ and $-9.8 \leq \log(\text{SSFR}/\text{yr}^{-1}) \leq -8.6$ respectively. The LIRG UVLGs have larger stellar masses and considerably higher SFR than either the Large or Compact UVLG samples as a whole. The LIRG UVLGs have similar SSFR to the Compact UVLG sample, the latter group being considered as local analogs to high-redshift Lyman Break Galaxies (LBGs; see Overzier et al. 2009).

4.2. Optical and UV-selected (U)LIRG Samples

Figures 3 and 4 show that, on average, (U)LIRGs with high SSFR have larger IRX and IR/UV and redder β than (U)LIRGs with lower SSFR, implying greater extinction by dust in the high SSFR systems. The GOALS sample spans the same range of SSFR as the UV-selected sample of Buat et al. (2009). However the UV-selected sample does not include galaxies with high IRX ($\log(\text{IRX}) \gtrsim 2.0$), which comprise 48% of the GOALS sample. The LIRGs in the LBG sample of Buat et al. (2009) include some systems similar to the GOALS UVLGs, while the majority have higher L_{UV} and low IRX.

The inverse of SSFR provides a doubling timescale for the stellar mass of a galaxy. The range for GOALS systems (excluding those with IRAC colors suggesting a possible AGN) is from 18 Gyr

to 290 Myr, with a median of 2.6 Gyr. Kaviraj (2009) fit double-burst star formation history models to a large sample of SDSS-selected LIRGs out to $z = 0.2$, finding average burst ages of 7 Gyr and 1 Gyr. The 43 systems in common between Kaviraj (2009) and the GOALS GALEX sample are consistent with being drawn from the same distribution in β and IRX as the entire GOALS GALEX sample.

4.3. Resolved Systems and Implications for Unresolved LIRGs at High Redshift

As emphasized by Charmandaris, Le Floch, & Mirabel (2004), individual galaxies in interacting systems can have very different far-infrared and UV properties leading to incorrect assumptions about the system as a whole when viewed as a single unresolved system (e.g. at high redshift). In particular, these authors note that the mid-IR/UV ratios of the components of the Arp 299 and VV 114 systems vary by well over an order of magnitude between the individual interacting galaxies. Our combined GALEX and Spitzer observations of the GOALS sample shows that this situation exists in a significant number of LIRG systems at low redshift. We define a source that produces at least twice as much luminosity as the companion to be dominant at that wavelength. Among LIRGs which can be resolved into interacting galaxies, approximately 32% consist of one galaxy which dominates the IR luminosity while a companion dominates the UV (hereafter referred to as “VV 114-like” systems). Extrapolating to number counts at $z \geq 1$ as in Charmandaris et al. (2004), this implies that as many as 15 – 30% of high redshift galaxies are unresolved VV 114-like systems.

In 21% of resolved systems, a single galaxy dominates both the IR and UV emission (such as Arp 182, for example). On average the ΔIRX value of the dominant galaxy is over four times larger than that of IR-dominant galaxies of similar UV color in a VV 114-like system. If we look at the masses of resolved pairs, the ΔIRX of the more massive galaxy is on average four times greater than that of the less massive galaxy. These are independent effects: the IR dominant galaxy in a resolved system is likely to dominate the mass of the system regardless of its contribution to the UV luminosity of the system. If we make the simplistic assumption that LIRG mergers form a single evolutionary sequence, our observations suggest that the phase in which the component galaxies have comparable IR and UV emission is 50% longer than the phase in which a single galaxy dominates both wavelengths. Furthermore, the fact that the high mass component is above the starburst relation would also be consistent with the fact that a synchronization of the nuclear starbursts in the two interacting galaxies is rare.

The ability to visualize merger simulations at observed wavelengths from the FUV to the FIR will facilitate the interpretation of data sets such as that presented in this paper. The SUNRISE code of Jonsson et al. (2006) may help answer outstanding questions such as: What types of mergers (and what fraction of viewing orientations) consist of an IR-dominant LIRG with a UV-dominant companion? What mergers consist of a LIRG which dominates both IR and UV relative to its companion? How long do these phases last? Do certain types of progenitor galaxies (Hubble type,

mass ratio, gas fraction, orbit, etc.) lead to different observables (IRX, $\beta(\text{GALEX})$, IR or UV fraction, SSFR, etc.) during the merger?

Although the different definitions of $\beta(\text{GALEX})$ preclude a direct comparison, the GOALS sample appears to be generally consistent with the merger simulations shown in Jonsson et al. (2006). In particular, the ULIRG simulations predict an IRX that is up to a factor of ten times greater than starburst galaxies with a narrow range of blue to intermediate UV colors. The GOALS ULIRGs within the same range of $\beta(\text{IUE})$ have a median ΔIRX of 0.9.

5. Conclusions

We present a comparison of the UV and infrared properties of 135 LIRGs and ULIRGs in the GOALS sample observed by GALEX and Spitzer. We find that:

- LIRGs have larger IR excesses than lower luminosity galaxies of similar UV color. On average, more luminous LIRGs and ULIRGs have larger IRX and redder colors.
- The contribution of the FUV to the measured SFR is on average 4%; UV emission alone is not a reliable indicator of the SFR for LIRGs.
- The median SSFR of the GOALS sample ($3.9 \times 10^{-10} \text{ yr}^{-1}$, corresponding to a mass doubling timescale of 2.6 Gyr) is approximately equal to the maximum SSFR seen in lower luminosity galaxies, however the median IR/UV ratio (39) for GOALS galaxies is more than an order of magnitude greater.
- Deviations from the starburst IRX- $\beta(\text{GALEX})$ relation ΔIRX increase with IR luminosity for $L_{\text{IR}} \gtrsim 10^{10} L_{\odot}$, with considerable scatter. LIRG systems with IRAC colors that may indicate the presence of an AGN have average IRX ratios a factor of six larger than the rest of the sample. ΔIRX is not strongly correlated with IRAS 25 $\mu\text{m}/60 \mu\text{m}$ color, IRAS 60 $\mu\text{m}/100 \mu\text{m}$ color, Spitzer 8 $\mu\text{m}/24 \mu\text{m}$ color, L_{FUV} , or 8 μm concentration (1 kpc/Total).
- A minimum of 19% of the total L_{IR} of the RBGS sample is produced in LIRGs and ULIRGs with $\beta > 0$, sources that are typically absent from UV-selected samples at high redshift. A minimum of 11% of the total L_{IR} of the RBGS sample is produced in LIRGs and ULIRGs with $\Delta\text{IRX} > 1$, an order of magnitude above the starburst relation.
- Using the starburst IRS- β relation to estimate L_{IR} from rest-frame UV observations of LIRGs and ULIRGs would underestimate L_{IR} by a factor of three on average, with a wide range (factors of 0.2–68) of possible under- or over estimates, particularly for red UV colors (large values of β) where L_{IR} could be overestimated by as much as a factor of 2400 using a linear extrapolation of the starburst relation.

- The UV and IR properties of GOALS systems are qualitatively consistent with an evolutionary picture in which some galaxies transition from LIRGs to ULIRGs over the course of a major merger event. More luminous galaxies, mergers, and galaxies with high SSFR are more heavily obscured than less luminous galaxies, non-mergers, and galaxies with lower SSFR.
- Among LIRG systems resolved into individual interacting galaxies, pairs in which one galaxy dominates the IR emission while the companion dominates UV emission (such as the well-studied LIRG system VV 114) are more common than pairs in which one galaxy dominates both wavelengths (32% and 21% of the sample, respectively). On average, galaxies which dominate both wavelengths have ΔIRX values four times larger than an IR-dominant galaxy in a “VV 114-like” system. The large fraction of “VV 114-like” systems has important implications for observations of interacting galaxies at high redshift in that the IR and UV properties of the unresolved systems can differ by over an order of magnitude from the properties of the component galaxies.

This research has made use of the NASA/IPAC Extragalactic Database (NED) which is operated by the Jet Propulsion Laboratory, California Institute of Technology, under contract with the National Aeronautics and Space Administration. This research has made use of the NASA/ IPAC Infrared Science Archive, which is operated by the Jet Propulsion Laboratory, California Institute of Technology, under contract with the National Aeronautics and Space Administration. Based on observations made with the NASA Galaxy Evolution Explorer. GALEX is operated for NASA by the California Institute of Technology under NASA contract NAS5-98034. VC acknowledges partial support from the EU ToK grant 39965 and FP7-REGPOT 206469. We thank Ranga Chary, Brian Siana, and Harry Teplitz for helpful discussions. We thank Armando Gil de Paz for making his GALEX background subtraction code available, Danny Dale for providing the SINGS data points in Fig. 3, and the anonymous referee for helpful comments.

A. UV Colors

The UV color of an object can be parameterized in several ways, complicating the comparison of results between different data sets. The UV continuum slope β was defined by Calzetti, Kinney, & Storchi-Bergman (1994) for use with IUE spectra. More recent photometric instruments such as STIS (Goldader et al. 2002) and GALEX cannot directly measure this spectroscopic β , referred to as $\beta(\text{IUE})$ in the main text of this paper and in Fig. 1. Instead the slope between a NUV data point and a FUV data point is measured and labeled β , referred to as $\beta(\text{GALEX})$. Some authors abandon the UV slope and instead measure a conventional color FUV-NUV, expressed in magnitudes (e.g., GDP).

Since 11 galaxies from Meurer et al. (1999) are included in GDP, we derive an empirical conversion between $\beta(\text{IUE})$ and $\beta(\text{GALEX})$:

$$\beta(\text{IUE}) = (-0.3 \pm 0.1) + (1.6 \pm 0.2)\beta(\text{GALEX}) \quad (\text{A1})$$

This conversion is not necessarily valid outside the range $-2 < \beta(\text{IUE}) < 0.5$ or $-1 < \beta(\text{GALEX}) < 0.5$.

REFERENCES

- Armus, L., et al. 2009, *PASP*, 121, 559
- Boquien, M., et al. 2009, *ApJ*, 706, 553
- Buat, V., Takeuchi, T. T., Burgarella, D., Giovannoli, E., & Murata, K. L. 2009, *A&A*, 507, 693
- Calzetti, D., Kinney, A. L., & Storchi-Bergmann, T. 1994, *ApJ*, 429, 582
- Caputi, K. I., Dole, H., Lagache, G., McLure, R. J., Dunlop, J. S., Puget, J.-L., Le Floch, E., & Pérez-González, P. G. 2006, *A&A*, 454, 143
- Charlot, S., & Fall, S. M. 2000, *ApJ*, 539, 718
- Charmandaris, V., Stacey, G. J., & Gull, G. 2002, *ApJ*, 571, 282
- Charmandaris, V., Le Floch, E., & Mirabel, I. F. 2004, *ApJ*, 600, L15
- Cortese, L., et al. 2006, *ApJ*, 637, 242
- Dale, D. A., & Helou, G. 2002, *ApJ*, 576, 159
- Dale, D. A., et al. 2007, *ApJ*, 655, 863
- de Vaucouleurs, G., de Vaucouleurs, A., Corwin, H. G., Jr., Buta, R. J., Paturel, G., & Fouque, P. 1991, Volume 1-3, XII, 2069 pp. 7 figs.. Springer-Verlag Berlin Heidelberg New York
- Genzel, R., Tacconi, L. J., Rigopoulou, D., Lutz, D., & Tecza, M. 2001, *ApJ*, 563, 527
- Gil de Paz, A., et al. 2007, *ApJS*, 173, 185 (GDP)
- Goldader, J. D., Meurer, G., Heckman, T. M., Seibert, M., Sanders, D. B., Calzetti, D., & Steidel, C. C. 2002, *ApJ*, 568, 651
- Heckman, T. M., et al. 2005, *ApJ*, 619, L35
- Iverson, R. J., Smail, I., Barger, A. J., Kneib, J.-P., Blain, A. W., Owen, F. N., Kerr, T. H., & Cowie, L. L. 2000, *MNRAS*, 315, 209
- Jonsson, P., Cox, T. J., Primack, J. R., & Somerville, R. S. 2006, *ApJ*, 637, 255

- Kaviraj, S. 2009, MNRAS, 394, 1167
- Kennicutt, R. C., Jr. 1998, ARA&A, 36, 189
- Kennicutt, R. C., Jr., et al. 2003, PASP, 115, 928
- Kong, X., Charlot, S., Brinchmann, J., & Fall, S. M. 2004, MNRAS, 349, 769
- Lacey, C. G., Baugh, C. M., Frenk, C. S., Silva, L., Granato, G. L., & Bressan, A. 2008, MNRAS, 385, 1155
- Le Flocc'h, E., et al. 2005, ApJ, 632, 169
- Leitherer, C., et al. 1999, ApJS, 123, 3
- Magnelli, B., Elbaz, D., Chary, R. R., Dickinson, M., Le Borgne, D., Frayer, D. T., & Willmer, C. N. A. 2009, A&A, 496, 57
- Magorrian, J., et al. 1998, AJ, 115, 2285
- Mazzarella, J., et al. 2010, AJ, in preparation
- Meurer, G. R., Heckman, T. M., & Calzetti, D. 1999, ApJ, 521, 64
- Muñoz-Mateos, J. C., et al. 2009, ApJ, 701, 1965
- Overzier, R. A., et al. 2009, ApJ, 706, 203
- Salpeter, E. E. 1955, ApJ, 121, 161
- Sanders, D. B., Soifer, B. T., Elias, J. H., Madore, B. F., Matthews, K., Neugebauer, G., & Scoville, N. Z. 1988, ApJ, 325, 74
- Sanders, D. B., Soifer, B. T., Elias, J. H., Neugebauer, G., & Matthews, K. 1988, ApJ, 328, L35
- Sanders, D. B., & Mirabel, I. F. 1996, ARA&A, 34, 749
- Sanders, D. B., Mazzarella, J. M., Kim, D.-C., Surace, J. A., & Soifer, B. T. 2003, AJ, 126, 1607
- Seibert, M., et al. 2005, ApJ, 619, L55
- Stern, D., et al. 2005, ApJ, 631, 163
- Surace, J. A., & Sanders, D. B. 2000, AJ, 120, 604
- Surace, J. A., Sanders, D. B., & Evans, A. S. 2000, ApJ, 529, 170
- Tacconi, L. J., Genzel, R., Lutz, D., Rigopoulou, D., Baker, A. J., Iserlohe, C., & Tecza, M. 2002, ApJ, 580, 73

Wyder, T. K., et al. 2005, ApJ, 619, L15

Table 1. GOALS GALEX Photometry - Integrated Systems

System (1)	Alternate Name (2)	RA (J2000) (3)	Dec (J2000) (4)	log(L _{IR}) (5)	t_{FUV} (6)	$f_{\nu}(FUV)$ (7)	σ_{FUV} (8)	t_{NUV} (9)	$f_{\nu}(NUV)$ (10)	σ_{NUV} (11)
NGC 0023		00h09m53.41s	+25° 55' 25.6''	11.12	3410	1.26E-14	8.E-17	3410	1.49E-14	3.E-17
NGC 0034		00h11m06.55s	-12° 06' 26.3''	11.49	119	1.53E-14	4.E-16	119	1.05E-14	2.E-16
Arp 256	MCG-02-01-051-2	00h18m50.40s	-10° 22' 08.0''	11.48	1618	2.65E-14	2.E-16	1618	2.50E-14	6.E-17
ESO 350-IG038		00h36m52.50s	-33° 33' 19.0''	11.28	3356.05	3.95E-14	1.E-16	3356.05	2.31E-14	4.E-17
NGC 0232		00h42m45.82s	-23° 33' 40.9''	11.44	115	2.65E-15	2.E-16	115	2.37E-15	1.E-16
MCG+12-02-001		00h54m03.61s	+73° 05' 11.8''	11.50	112	3.60E-16	3.E-16	112	1.61E-16	1.E-16
NGC 0317B		00h57m41.67s	+43° 47' 33.2''	11.19	110	2.36E-15	3.E-16	110	4.29E-15	1.E-16
IC 1623	VV 114	01h07m47.18s	-17° 30' 25.3''	11.71	1668	6.40E-14	2.E-16	1668	4.87E-14	8.E-17
MCG-03-04-014		01h10m08.96s	-16° 51' 09.8''	11.65	3241	3.63E-15	5.E-17	3241	3.78E-15	2.E-17
ESO 244-G012		01h18m08.10s	-44° 27' 51.0''	11.38	117	8.88E-15	4.E-16	117	7.59E-15	1.E-16
CGCG 436-030		01h20m02.72s	+14° 21' 42.9''	11.69	3178.05	6.42E-15	6.E-17	6101.5	8.68E-15	2.E-17
IRAS F01364-1042		01h38m52.92s	-10° 27' 11.4''	11.85	3284	2.50E-16	3.E-17	3753	7.62E-16	1.E-17
NGC 0695		01h51m14.24s	+22° 34' 56.5''	11.68	3403	4.96E-15	6.E-17	6404	6.83E-15	2.E-17
UGC 01385		01h54m53.79s	+36° 55' 04.6''	11.05	137	1.09E-14	4.E-16	137	8.60E-15	1.E-16
NGC 0877		02h17m59.64s	+14° 32' 38.6''	11.10	1694	2.81E-14	2.E-16	1694	2.68E-14	6.E-17
MCG+05-06-036		02h23m20.45s	+32° 11' 34.2''	11.64	147	2.29E-15	2.E-16	147	3.52E-15	8.E-17
NGC 0958		02h30m42.58s	-02° 56' 27.2''	11.20	1696	1.41E-14	1.E-16	1696	1.27E-14	4.E-17
NGC 1068		02h42m40.71s	-00° 00' 47.8''	11.40	1627	2.86E-13	5.E-16	1627	2.64E-13	2.E-16
UGC 02238		02h46m17.49s	+13° 05' 44.4''	11.33	1316	1.42E-15	7.E-17	1400	1.28E-15	3.E-17
IRAS F02437+2122		02h46m39.15s	+21° 35' 10.3''	11.16	120	120	3.83E-16	9.E-17
NGC 1275		03h19m48.16s	+41° 30' 42.1''	11.26	14563.35	1.78E-14	5.E-17	17097.35	1.67E-14	2.E-17
NGC 1365		03h33m36.37s	-36° 08' 25.4''	11.00	1662.05	1.14E-13	5.E-16	1662.05	1.05E-13	2.E-16
IRAS F03359+1523		03h38m46.70s	+15° 32' 55.0''	11.55	107	9.11E-16	3.E-16	107	1.32E-15	6.E-17
CGCG 465-012		03h54m16.08s	+15° 55' 43.4''	11.20	133	3.49E-16	3.E-16	133	1.68E-15	1.E-16
IRAS 03582+6012		04h02m30.65s	+60° 20' 33.4''	11.43	116	116	8.08E-17	1.E-16
UGC 02982		04h12m22.45s	+05° 32' 50.6''	11.20	113	4.51E-16	4.E-16	113	2.46E-16	1.E-16
ESO 550-IG025		04h21m20.00s	-18° 48' 48.0''	11.51	129	2.68E-15	3.E-16	129	2.80E-15	1.E-16
IRAS 04271+3849		04h30m33.09s	+38° 55' 47.7''	11.11	166	166
ESO 203-IG001		04h46m49.50s	-48° 33' 32.9''	11.86	3899	7.39E-16	3.E-17	5482	6.81E-16	1.E-17
MCG-05-12-006		04h52m04.96s	-32° 59' 25.6''	11.17	81	1.64E-15	3.E-16	81	3.94E-15	1.E-16
CGCG 468-002		05h08m20.50s	+17° 21' 58.0''	11.22	118	7.51E-16	5.E-16	118	5.07E-16	1.E-16
IRAS 05083+2441		05h11m25.88s	+24° 45' 18.3''	11.26	111.05	2.00E-16	2.E-16	111.05	3.42E-16	6.E-17
IRAS 05129+5128		05h16m56.10s	+51° 31' 56.5''	11.42	130	5.33E-16	3.E-16	130	5.90E-16	1.E-16
IRAS F05189-2524		05h21m01.47s	-25° 21' 45.4''	12.16	2310.05	1.58E-15	8.E-17	2311.05	1.36E-15	3.E-17
IRAS 05223+1908		05h25m16.50s	+19° 10' 46.0''	11.65	114	114
MCG+08-11-002		5h40m43.68s	+49° 41' 35.4''	11.46	3368	3368	8.60E-16	2.E-17
NGC 1961		05h42m04.80s	+69° 22' 43.3''	11.06	3932.05	2.86E-14	1.E-16	3932.05	2.69E-14	5.E-17
UGC 03410		06h14m29.63s	+80° 26' 59.6''	11.10	136	3.20E-15	3.E-16	137	2.94E-15	1.E-16
NGC 2146		06h18m37.71s	+78° 21' 25.3''	11.12	1621	1.39E-14	1.E-16	1621	1.93E-14	6.E-17
ESO255-IG007		6h27m22.64s	-47° 10' 48.4''	11.90	3393	5.46E-15	6.E-17	3393	5.21E-15	2.E-17
NGC 2342		07h09m18.08s	+20° 38' 09.5''	11.31	111	2.54E-14	6.E-16	111	2.26E-14	2.E-16
NGC 2369		07h16m37.73s	-62° 20' 37.4''	11.16	105	5.13E-15	4.E-16	105	4.72E-15	1.E-16
NGC 2388		07h28m53.44s	+33° 49' 08.7''	11.28	1700	2.96E-14	2.E-16	1700	2.19E-14	6.E-17
MCG+02-20-003		07h35m43.37s	+11° 42' 33.5''	11.13	117	1.16E-14	4.E-16	117	9.14E-15	2.E-16
NGC 2623		08h38m24.08s	+25° 45' 16.9''	11.60	1698	5.44E-15	8.E-17	1698	4.93E-15	3.E-17
ESO 060-IG016		8h52m32.03s	-69° 01' 57.3''	11.82	1580	1.11E-15	1.E-16	1580	1.65E-15	4.E-17
IRAS F08572+3915		09h00m25.39s	+39° 03' 54.4''	12.16	1268.1	1.39E-15	6.E-17	1268.1	1.94E-15	3.E-17
IRAS 09022-3615		09h04m12.70s	-36° 27' 01.1''	12.31	5224	2.38E-16	6.E-17	5224	1.11E-15	2.E-17
IRAS F09111-1007		09h13m38.80s	-10° 19' 20.3''	12.06	2924	1.07E-15	5.E-17	19292.1	1.84E-15	8.E-18
UGC 04881		09h15m55.10s	+44° 19' 55.0''	11.74	3338	2.52E-15	4.E-17	3339	3.42E-15	2.E-17
UGC 05101		09h35m51.65s	+61° 21' 11.3''	12.01	1690	8.91E-16	5.E-17	1690	1.29E-15	2.E-17
MCG+08-18-013		09h36m37.19s	+48° 28' 27.7''	11.34	105	9.76E-15	4.E-16	105	6.49E-15	1.E-16
Arp 303	IC 0563-4	09h46m20.60s	+03° 03' 30.0''	11.23	118	4.65E-15	3.E-16	118	4.24E-15	1.E-16
NGC 3110		10h04m02.11s	-06° 28' 29.2''	11.37	80	1.80E-14	6.E-16	80	1.67E-14	2.E-16
ESO 374-IG032	IRAS F10038-3338	10h06m04.80s	-33° 53' 15.0''	11.78	4930.65	2.28E-15	5.E-17	14429.75	7.91E-15	1.E-17
IRAS F10173+0828		10h20m00.22s	+08° 13' 34.0''	11.86	3284.2	5.87E-18	3.E-17	6789.2	9.63E-16	1.E-17
NGC 3221		10h22m19.90s	+21° 34' 30.4''	11.09	107	7.79E-15	4.E-16	107	8.36E-15	2.E-16
NGC 3256		10h27m51.83s	-43° 54' 13.2''	11.64	1152	3.10E-14	2.E-16	1152	3.72E-14	9.E-17
ESO 264-G036		10h43m07.67s	-46° 12' 44.6''	11.32	109	7.74E-17	4.E-16	109	2.70E-15	1.E-16
IRAS F10565+2448		10h59m18.28s	+24° 32' 34.8''	12.08	1653	4.00E-16	4.E-17	1653	9.22E-16	2.E-17
MCG+07-23-019		11h03m53.20s	+40° 50' 57.0''	11.62	105	7.27E-15	3.E-16	3733	5.19E-15	2.E-17
CGCG 011-076		11h21m12.26s	-02° 59' 03.5''	11.43	106	5.90E-16	1.E-16	106	9.41E-16	6.E-17
IRAS F11231+1456	IC 2810	11h25m45.05s	+14° 40' 35.9''	11.64	122	1.55E-15	1.E-16	122	2.26E-15	7.E-17
NGC 3690	Arp 299	11h28m32.20s	+58° 33' 44.0''	11.93	103	1.19E-13	1.E-15	103	8.09E-14	4.E-16
ESO 320-G030		11h53m11.72s	-39° 07' 48.9''	11.17	103	3.79E-15	4.E-16	103	4.94E-15	1.E-16
ESO 440-IG058		12h06m51.90s	-31° 56' 54.0''	11.43	92	2.26E-15	3.E-16	92	3.48E-15	1.E-16

Table 1—Continued

System (1)	Alternate Name (2)	RA (J2000) (3)	Dec (J2000) (4)	$\log(L_{\text{IR}})$ (5)	t_{FUV} (6)	f_{ν} (FUV) (7)	σ_{FUV} (8)	t_{NUV} (9)	f_{ν} (NUV) (10)	σ_{NUV} (11)
IRAS F12112+0305		12h13m46.00s	+02°48′38.0″	12.36	3713	1.46E-15	3.E-17	3713	1.14E-15	2.E-17
ESO 267-G030		12h14m12.84s	-47°13′43.2″	11.25	104	2.29E-15	4.E-16	104	2.23E-15	1.E-16
NGC 4922		13h01m24.90s	+29°18′40.0″	11.38	1888.7	1.40E-15	5.E-17	3524	2.19E-15	2.E-17
CGCG 043-099		13h01m50.80s	+04°20′00.0″	11.68	137	1.69E-15	2.E-16	137	1.36E-15	8.E-17
MCG-02-33-098-9		13h02m19.70s	-15°46′03.0″	11.17	102	5.51E-15	4.E-16	112	7.11E-15	1.E-16
ESO 507-G070		13h02m52.35s	-23°55′17.7″	11.56	1251	2.02E-15	9.E-17	1251	1.99E-15	3.E-17
VV 250a		13h15m35.02s	+62°07′28.8″	11.81	103	8.66E-15	4.E-16	120	8.87E-15	1.E-16
UGC 08387		13h20m35.34s	+34°08′22.2″	11.73	119	4.13E-15	3.E-16	119	4.65E-15	1.E-16
NGC 5104		13h21m23.08s	+00°20′32.7″	11.27	113	2.97E-15	2.E-16	120	2.89E-15	1.E-16
MCG-03-34-064		13h22m24.45s	-16°43′42.4″	11.19	110	3.13E-15	3.E-16	110	3.16E-15	6.E-16
NGC 5135		13h25m44.06s	-29°50′01.2″	11.30	108	1.80E-14	6.E-16	108	1.96E-14	2.E-16
IC 4280		13h32m53.40s	-24°12′25.7″	11.15	116	9.92E-15	4.E-16	116	1.17E-14	2.E-16
NGC 5256		13h38m17.50s	+48°16′37.0″	11.56	111	1.02E-14	4.E-16	111	9.45E-15	2.E-16
Arp 240	NGC 5257-8	13h39m55.20s	+00°50′13.0″	11.62	129	3.94E-14	7.E-16	130	3.08E-14	2.E-16
UGC 08739		13h49m13.93s	+35°15′26.8″	11.15	59	6.46E-15	4.E-16	59	4.76E-15	2.E-16
NGC 5331		13h52m16.20s	+02°06′16.0″	11.66	2704	5.21E-15	6.E-17	4312.5	5.23E-15	2.E-17
Arp 84	NGC 5394-5	13h58m35.80s	+37°26′20.0″	11.08	91	7.52E-15	4.E-16	1476	8.88E-15	4.E-17
CGCG 247-020		14h19m43.25s	+49°14′11.7″	11.39	105	4.67E-16	2.E-16	105	3.59E-16	7.E-17
NGC 5653		14h30m10.42s	+31°12′55.8″	11.13	92	1.84E-14	6.E-16	92	1.85E-14	2.E-16
IRAS F14348-1447		14h37m38.37s	-15°00′22.8″	12.39	1942	1.32E-15	7.E-17	3134	9.46E-16	2.E-17
NGC 5734		14h45m09.05s	-20°52′13.7″	11.15	128	1.06E-14	4.E-16	128	9.61E-15	2.E-16
VV 340a		14h57m00.68s	+24°37′02.7″	11.74	3042	5.72E-15	6.E-17	6028	4.89E-15	2.E-17
CGCG 049-057		15h13m13.10s	+07°13′31.8″	11.35	88	7.87E-17	2.E-16	88	9.31E-16	9.E-17
VV 705		15h18m06.34s	+42°44′36.7″	11.92	110	5.23E-15	3.E-16	110	4.14E-15	1.E-16
IRAS F15250+3608		15h26m59.40s	+35°58′37.5″	12.08	168	2.42E-15	2.E-16	1601	2.25E-15	2.E-17
NGC 5936		15h30m00.84s	+12°59′21.5″	11.14	106	2.38E-14	6.E-16	106	2.01E-14	2.E-16
UGC 09913	Arp 220	15h34m57.11s	+23°30′11.5″	12.28	92	2.02E-15	3.E-16	92	3.07E-15	8.E-17
NGC 5990		15h46m16.37s	+02°24′55.7″	11.13	109	1.08E-14	4.E-16	109	9.97E-15	2.E-16
NGC 6052		16h05m12.90s	+20°32′32.0″	11.09	97	3.71E-14	8.E-16	2137	2.70E-14	5.E-17
NGC 6090		16h11m40.70s	+52°27′24.0″	11.58	2383	1.38E-14	1.E-16	14866.05	1.28E-14	1.E-17
IRAS F16164-0746		16h19m11.76s	-07°54′04.5″	11.62	3878	1.51E-15	1.E-16	3878	1.26E-15	3.E-17
CGCG 052-037		16h30m56.54s	+04°04′58.4″	11.45	115	1.55E-15	2.E-16	115	1.85E-15	9.E-17
NGC 6240		16h52m58.89s	+02°24′03.4″	11.93	108	6.39E-15	5.E-16	17086.45	6.40E-15	1.E-17
NGC 6286		16h58m31.38s	+58°56′10.5″	11.37	122	7.32E-15	3.E-16	122	6.46E-15	1.E-16
IRAS F17132+5313		17h14m20.00s	+53°10′30.0″	11.96	3116.75	1.44E-15	4.E-17	5577.65	1.67E-15	1.E-17
IRAS F17207-0014		17h23m22.16s	-00°17′01.7″	12.46	4345	1.19E-17	4.E-17	4345	8.07E-17	1.E-17
UGC 11041		17h54m51.82s	+34°46′34.4″	11.11	114	4.74E-15	3.E-16	114	3.76E-15	1.E-16
CGCG 141-034		17h56m56.63s	+24°01′01.6″	11.20	112	1.01E-15	3.E-16	112	5.26E-16	1.E-16
NGC 6621		18h12m55.31s	+68°21′48.4″	11.29	102	5.64E-15	3.E-16	102	6.14E-15	1.E-16
IC 4687		18h13m39.63s	-57°43′31.3″	11.62	145	1.74E-14	4.E-16	145	1.43E-14	2.E-16
NGC6670AB		18h33m35.60s	+59°53′20.0″	11.65	2760	3.06E-15	6.E-17	3531	3.29E-15	2.E-17
IC 4734		18h38m25.70s	-57°29′25.6″	11.35	112	8.06E-15	4.E-16	112	6.02E-15	1.E-16
ESO 593-IG008		19h14m30.90s	-21°19′07.0″	11.93	82	2.51E-15	5.E-16	4422	5.54E-15	3.E-17
IRAS F19297-0406		19h32m21.25s	-03°59′56.3″	12.45	98.75	1.72E-17	7.E-18	3802	2.06E-17	4.E-18
ESO 339-G011		19h57m37.54s	-37°56′08.4″	11.20	113	2.08E-15	3.E-16	113	2.86E-15	1.E-16
NGC 6907		20h25m06.65s	-24°48′33.5″	11.11	1686	8.18E-14	3.E-16	2175	6.30E-14	8.E-17
NGC 6926		20h33m06.11s	-02°01′39.0″	11.32	119	1.41E-14	5.E-16	119	1.02E-14	2.E-16
CGCG 448-020	II Zw 096	20h57m23.29s	+17°07′34.3″	11.94	66	1.64E-14	6.E-16	66	1.02E-14	2.E-16
ESO 286-IG019		20h58m26.79s	-42°39′00.3″	12.06	2974	5.51E-15	6.E-17	8100.05	5.06E-15	1.E-17
ESO 286-G035		21h04m11.18s	-43°35′33.0″	11.20	105	4.35E-15	3.E-16	105	4.72E-15	1.E-16
ESO 343-IG013		21h36m11.00s	-38°32′37.0″	11.14	81	3.95E-15	3.E-16	81	4.24E-15	1.E-16
NGC 7130		21h48m19.50s	-34°57′04.7″	11.42	1692	2.11E-14	1.E-16	1692	2.42E-14	6.E-17
IC 5179		22h16m09.10s	-36°50′37.4″	11.24	86	3.36E-14	8.E-16	86	3.17E-14	3.E-16
ESO 602-G025		22h31m25.48s	-19°02′04.1″	11.34	62	3.63E-15	4.E-16	62	3.38E-15	2.E-16
UGC 12150		22h41m12.26s	+34°14′57.0″	11.35	167	9.13E-17	2.E-16	167	8.54E-16	8.E-17
IRAS F22491-1808		22h51m49.26s	-17°52′23.5″	12.20	1696	1.89E-15	6.E-17	1696	2.04E-15	3.E-17
NGC 7469		23h03m15.62s	+08°52′26.4″	11.65	3768	4.50E-14	1.E-16	3768	3.29E-14	4.E-17
CGCG 453-062		23h04m56.53s	+19°33′08.0″	11.38	113	7.51E-16	2.E-16	113	1.29E-15	9.E-17
ESO 148-IG002		23h15m46.78s	-59°03′15.6″	12.06	3009.05	5.88E-15	6.E-17	5350.05	5.22E-15	2.E-17
IC 5298		23h16m00.70s	+25°33′24.1″	11.60	113	2.21E-15	3.E-16	113	1.76E-15	1.E-16
NGC 7552		23h16m10.77s	-42°35′05.4″	11.11	4825	7.33E-14	1.E-16	7560.95	8.68E-14	5.E-17
NGC 7592		23h18m22.54s	-04°24′58.5″	11.40	107	2.32E-14	6.E-16	107	1.38E-14	2.E-16
ESO 077-IG014		23h21m04.30s	-69°12′54.0″	11.76	2060	5.34E-16	5.E-17	6625.05	1.03E-15	1.E-17
NGC 7674		23h27m56.72s	+08°46′44.5″	11.56	1666	1.42E-14	1.E-16	1666	1.16E-14	4.E-17
IRAS F23365+3604		23h39m01.27s	+36°21′08.7″	12.20	3876	6.02E-16	5.E-17	3876	2.62E-15	2.E-17
MCG-01-60-022		23h41m54.10s	-03°38′29.0″	11.27	1489	7.28E-15	9.E-17	1489	5.50E-15	3.E-17

Table 1—Continued

System (1)	Alternate Name (2)	RA (J2000) (3)	Dec (J2000) (4)	$\log(L_{\text{IR}})$ (5)	t_{FUV} (6)	$f_{\nu}(\text{FUV})$ (7)	σ_{FUV} (8)	t_{NUV} (9)	$f_{\nu}(\text{NUV})$ (10)	σ_{NUV} (11)
Arp 86	NGC 7752-3	23h47m01.63s	+29°28′17.2″	11.07	1687.7	1.02E-14	1.E-16	3246	9.15E-15	3.E-17
NGC 7771		23h51m24.88s	+20°06′42.6″	11.40	8579	3.39E-14	8.E-17	16457	2.35E-14	2.E-17
MRK0331		23h51m26.80s	+20°35′09.9″	11.50	1129	2.91E-15	1.E-16	1129	3.07E-15	4.E-17

Note. — Column (1): System name, following the naming convention of Armus et al. (2009). Column (2): Alternate system name. Column (3): The best available source right ascension (J2000) in NED as of October 2008. Column (4): The best available source declination (J2000) in NED as of October 2008. Column (5): The total infrared luminosity in \log_{10} Solar units computed using the IRAS flux densities reported in the RBGS and the luminosity distances in Armus et al. (2009). Column (6): GALEX FUV integration time in seconds. Column (7): GALEX FUV flux density in units of $\text{erg s}^{-1}\text{cm}^{-2}\text{\AA}^{-1}$. Column (8): GALEX FUV flux density uncertainty. Column(9): GALEX NUV integration time in seconds. Column (10): GALEX NUV flux density in units of $\text{erg s}^{-1}\text{cm}^{-2}\text{\AA}^{-1}$. Column (11): GALEX NUV flux density uncertainty.

Table 2. GALEX Photometry - Resolved Components

System Name (1)	Galaxy Name (2)	RA (J2000) (3)	Dec (J2000) (4)	$\log(L_{\text{IR}})$ (5)	$f_{\nu}(\text{FUV})$ (6)	σ_{FUV} (7)	$f_{\nu}(\text{NUV})$ (8)	σ_{NUV} (9)
GOALS J001108.5-120351	NGC 0034	00h11m06.56s	-12°06'28.2''	11.34	1.53E-14	4.E-16	1.05E-14	6.E-16
GOALS J001108.5-120351	NGC 0035	00h11m10.51s	-12°01'14.9''	10.57	6.92E-15	3.E-16	8.63E-15	6.E-16
MCG-02-01-051-2	MCG-02-01-052	00h18m49.85s	-10°21'34.0''	10.36	1.24E-14	1.E-16	1.05E-14	1.E-16
MCG-02-01-051-2	MCG-02-01-051	00h18m50.90s	-10°22'36.7''	11.45	1.42E-14	1.E-16	1.08E-14	1.E-16
NGC 0232	NGC 0232	00h42m45.83s	-23°33'41.0''	11.37	2.65E-15	2.E-16	2.37E-15	5.E-16
NGC 0232	NGC 0235A	00h42m52.82s	-23°32'27.8''	10.86	1.28E-15	2.E-16	1.19E-15	5.E-16
NGC 0317	NGC 0317A	00h57m39.04s	+43°48'03.1''	8.96	2.48E-16	3.E-17	1.37E-15	4.E-17
NGC 0317	NGC 0317B	00h57m40.41s	+43°47'32.5''	11.19	2.12E-15	3.E-16	2.91E-15	9.E-17
IC 1623	IC 1623A	01h07m46.75s	-17°30'26.2''	11.08	6.16E-14	2.E-16	4.57E-14	7.E-17
IC 1623	IC 1623B	01h07m47.54s	-17°30'25.1''	11.59	2.31E-15	8.E-18	3.03E-15	5.E-18
ESO 244-G012	ESO 244-G012 NED01	01h18m08.23s	-44°28'00.4''	9.49	7.27E-15	3.E-16	5.61E-15	1.E-16
ESO 244-G012	ESO 244-G012 NED02	01h18m08.31s	-44°27'43.4''	11.37	1.61E-15	6.E-17	1.98E-15	3.E-17
GOALS J015457.8+365508	UGC 01385	01h54m53.82s	+36°55'04.3''	11.00	1.92E-15	2.E-16	1.71E-15	3.E-16
GOALS J015457.8+365508	KUG 0152+366	01h55m01.75s	+36°55'11.6''	10.05	8.94E-15	3.E-16	6.89E-15	4.E-16
GOALS J021756.5+143158	NGC 0876	02h17m53.26s	+14°31'18.4''	10.51	2.81E-14	2.E-16	2.68E-14	2.E-16
GOALS J021756.5+143158	NGC 0877	02h17m59.68s	+14°32'38.2''	11.07	1.27E-15	6.E-17	1.31E-15	2.E-16
MRK1034	MCG+05-06-035	02h23m18.97s	+32°11'18.5''	11.00	1.61E-15	1.E-16	2.53E-15	6.E-17
MRK1034	MCG+05-06-036	02h23m21.99s	+32°11'48.8''	11.53	6.80E-16	5.E-17	9.82E-16	2.E-17
KPG 095	UGC 02894	03h54m07.67s	+15°59'24.3''	10.81	1.56E-15	3.E-16	1.36E-15	7.E-16
KPG 095	CGCG 465-012	03h54m15.95s	+15°55'43.4''	11.16	3.49E-16	3.E-16	1.68E-15	7.E-16
ESO 550-IG025	ESO 550-IG025 NED01	04h21m20.02s	-18°48'39.6''	11.27	2.18E-15	2.E-16	2.17E-15	8.E-17
ESO 550-IG025	ESO 550-IG025 NED02	04h21m20.08s	-18°48'57.4''	11.13	5.00E-16	5.E-17	6.30E-16	2.E-17
CGCG 468-002	CGCG 468-002 NED01	05h08m19.71s	+17°21'47.8''	10.74	4.20E-17	3.E-17	2.65E-16	7.E-17
CGCG 468-002	CGCG 468-002 NED02	05h08m21.21s	+17°22'08.0''	11.05	7.09E-16	4.E-16	2.42E-16	6.E-17
GOALS J051127.4+244539	IRAS 05083+2441	05h11m25.88s	+24°45'18.2''	11.24	1.99E-16	2.E-16	3.15E-16	4.E-16
GOALS J051127.4+244539	2MASX J05112888+2445593	05h11m29.05s	+24°46'04.0''	10.06	1.02E-18	2.E-16	2.66E-17	4.E-16
KPG 108	UGC 03405	06h13m57.90s	+80°28'34.7''	10.54	3.20E-15	3.E-16	2.94E-15	5.E-16
KPG 108	UGC 03410	06h14m29.61s	+80°26'59.6''	11.02	1.04E-15	2.E-16	1.12E-15	5.E-16
KPG 125	NGC 2341	07h09m12.01s	+20°36'11.2''	11.11	4.98E-15	4.E-16	6.98E-15	8.E-16
KPG 125	NGC 2342	07h09m18.07s	+20°38'10.2''	11.20	2.54E-14	6.E-16	2.26E-14	9.E-16
WBL 142	NGC 2385	07h28m28.17s	+33°50'16.9''	9.59	3.22E-16	6.E-17	1.86E-15	2.E-16
WBL 142	NGC 2388	07h28m53.44s	+33°49'07.8''	11.26	2.96E-14	2.E-16	2.19E-14	2.E-16
WBL 142	NGC 2389	07h29m04.59s	+33°51'38.0''	10.65	7.20E-17	6.E-17	3.62E-16	2.E-16
GOALS J073542.4+113938	NGC 2416	07h35m41.53s	+11°36'42.1''	...	1.16E-14	4.E-16	9.14E-15	7.E-16
GOALS J073542.4+113938	MCG+02-20-003	07h35m43.44s	+11°42'34.8''	...	5.73E-15	3.E-16	7.78E-15	7.E-16
IRAS F09111-1007	2MASX J09133644-1019296	09h13m36.50s	-10°19'29.7''	11.90	3.10E-17	1.E-17	9.30E-17	8.E-18
IRAS F09111-1007	2MASX J09133888-1019196	09h13m38.89s	-10°19'19.6''	11.24	1.10E-15	3.E-17	1.75E-15	4.E-19
UGC 04881	UGC 04881 NED02	09h15m54.69s	+44°19'50.8''	11.26	6.89E-17	6.E-18	9.72E-17	3.E-18
UGC 04881	UGC 04881 NED01	09h15m55.52s	+44°19'57.4''	11.56	1.69E-16	9.E-18	2.34E-16	4.E-18
CGCG 239-011	CGCG 239-011 NED01	09h36m30.86s	+48°28'09.9''	9.93	6.88E-15	3.E-16	3.84E-15	3.E-16
CGCG 239-011	MCG+08-18-013	09h36m37.20s	+48°28'27.7''	11.32	2.88E-15	2.E-16	2.65E-15	3.E-16
GOALS J112110.3-025922	2MASX J11210825-0259399	11h21m08.29s	-02°59'39.2''	10.02	2.98E-16	1.E-16	2.40E-16	3.E-16
GOALS J112110.3-025922	CGCG 011-076	11h21m12.24s	-02°59'02.5''	11.41	2.92E-16	1.E-16	7.01E-16	3.E-16
IC 2810	IC 2810A	11h25m45.07s	+14°40'36.0''	11.45	1.43E-15	1.E-16	2.10E-15	3.E-16
IC 2810	IC 2810B	11h25m49.55s	+14°40'06.6''	11.20	1.28E-16	7.E-17	1.62E-16	2.E-16
Arp 299	NGC 3690	11h28m31.04s	+58°33'40.5''	11.77	8.32E-14	9.E-16	5.79E-14	3.E-16
Arp 299	IC 0694	11h28m33.67s	+58°33'46.1''	11.41	3.59E-14	4.E-16	2.30E-14	1.E-16
ESO 440-IG058	ESO 440-IG058 NED01	12h06m51.70s	-31°56'46.4''	10.54	1.63E-15	2.E-16	2.43E-15	9.E-17
ESO 440-IG058	ESO 440-IG058 NED02	12h06m51.87s	-31°56'59.2''	11.37	6.34E-16	9.E-17	1.05E-15	4.E-17
SGC 1211-470	ESO 267-G029	12h13m52.28s	-47°16'25.4''	11.18	5.66E-15	5.E-16	4.23E-15	9.E-16
SGC 1211-470	ESO 267-G030	12h14m12.81s	-47°13'42.5''	11.23	2.29E-15	4.E-16	2.23E-15	8.E-16
NGC 4922	NGC 4922 NED01	13h01m24.51s	+29°18'29.8''	8.87	3.55E-16	1.E-17	8.25E-16	6.E-18
NGC 4922	NGC 4922 NED02	13h01m25.27s	+29°18'49.5''	11.38	1.04E-15	3.E-17	1.37E-15	1.E-17
MCG-02-33-098-9	MCG-02-33-098	13h02m19.66s	-15°46'04.2''	11.00	1.39E-15	9.E-17	3.22E-15	7.E-17
MCG-02-33-098-9	MCG-02-33-099	13h02m20.38s	-15°45'59.6''	10.66	4.11E-15	3.E-16	3.89E-15	8.E-17
VV 250	VV 250b	13h15m30.69s	+62°07'45.8''	...	2.92E-15	1.E-16	2.80E-15	4.E-17
VV 250	VV 250a	13h15m34.96s	+62°07'29.2''	...	5.74E-15	3.E-16	6.06E-15	1.E-16
NGC 5256	MRK 266B	13h38m17.25s	+48°16'32.9''	11.37	4.38E-15	2.E-16	4.00E-15	7.E-17
NGC 5256	MRK 266A	13h38m17.79s	+48°16'41.6''	11.11	5.80E-15	2.E-16	5.45E-15	9.E-17
Arp 240	NGC 5257	13h39m52.95s	+00°50'25.9''	11.31	1.10E-14	4.E-16	9.63E-15	4.E-16
Arp 240	NGC 5258	13h39m57.72s	+00°49'53.0''	11.32	2.84E-14	6.E-16	2.11E-14	5.E-16
NGC 5331	NGC 5331 NED01	13h52m16.21s	+02°06'05.1''	11.54	1.32E-15	2.E-17	1.59E-15	6.E-18
NGC 5331	NGC 5331 NED02	13h52m16.43s	+02°06'30.9''	11.02	3.89E-15	5.E-17	3.64E-15	1.E-17
GOALS J144510.0-205331	NGC 5734	14h45m09.04s	-20°52'13.2''	11.04	2.64E-15	3.E-16	4.03E-15	7.E-16
GOALS J144510.0-205331	NGC 5743	14h45m11.02s	-20°54'48.6''	10.86	1.06E-14	4.E-16	9.61E-15	7.E-16
VV 340	VV 340b	14h57m00.32s	+24°36'24.6''	10.83	3.48E-15	4.E-17	2.96E-15	1.E-17

Table 2—Continued

System Name (1)	Galaxy Name (2)	RA (J2000) (3)	Dec (J2000) (4)	$\log(L_{\text{IR}})$ (5)	$f_{\nu}(\text{FUV})$ (6)	σ_{FUV} (7)	$f_{\nu}(\text{NUV})$ (8)	σ_{NUV} (9)
VV 340	VV 340a	14h57m00.70s	+24°37′05.8″	11.69	1.02E-15	2.E-17	8.53E-16	6.E-18
Arp 293	NGC 6285	16h58m23.99s	+58°57′21.7″	10.72	3.80E-15	2.E-16	3.47E-15	3.E-16
Arp 293	NGC 6286	16h58m31.63s	+58°56′13.3″	11.36	3.52E-15	2.E-16	2.99E-15	3.E-16
UGC 11175	NGC 6621	18h12m55.39s	+68°21′48.2″	11.28	1.86E-15	9.E-17	2.93E-15	5.E-17
UGC 11175	NGC 6621 SE	18h12m58.52s	+68°21′29.4″	9.52	3.63E-15	2.E-16	2.73E-15	5.E-17
UGC 11175	NGC 6622	18h12m59.68s	+68°21′15.1″	9.23	1.48E-16	7.E-18	4.79E-16	9.E-18
KTS57	IC 4686	18h13m38.77s	−57°43′57.3″	11.02	1.13E-14	3.E-16	1.08E-14	1.E-16
KTS57	IC 4687	18h13m39.80s	−57°43′30.7″	11.32	4.11E-15	1.E-16	3.52E-15	4.E-17
KTS57	IC 4689	18h13m40.38s	−57°44′54.3″	11.02	1.92E-15	2.E-16	1.51E-15	4.E-16
NGC 6670AB	NGC 6670B	18h33m32.77920s	+59°53′11.7″	11.32	7.77E-16	2.E-17	8.71E-16	9.E-18
NGC 6670AB	NGC 6670A	18h33m37.66800s	+59°53′21.3″	11.38	1.86E-15	3.E-17	1.73E-15	1.E-17
ESO 343-IG013	ESO 343-IG013 NED01	21h36m10.53s	−38°32′42.8″	10.60	2.63E-15	2.E-16	2.76E-15	9.E-17
ESO 343-IG013	ESO 343-IG013 NED02	21h36m10.93s	−38°32′33.0″	10.99	1.32E-15	1.E-16	1.49E-15	5.E-17
Arp 298	NGC 7469	23h03m15.64s	+08°52′25.5″	11.58	4.32E-14	1.E-16	3.11E-14	1.E-16
Arp 298	IC 5283	23h03m18.04s	+08°53′36.5″	10.79	1.77E-15	3.E-17	1.76E-15	5.E-17
NGC 7592	NGC 7592A	23h18m21.78s	−04°24′57.0″	11.17	2.35E-15	6.E-17	1.66E-15	2.E-17
NGC 7592	NGC 7592B	23h18m22.60s	−04°24′58.0″	11.01	2.09E-14	5.E-16	1.21E-14	2.E-16
ESO 077-IG014	ESO 077-IG014 NED01	23h21m03.73s	−69°13′01.0″	11.33	5.08E-16	4.E-17	8.42E-16	9.E-18
ESO 077-IG014	ESO 077-IG014 NED02	23h21m05.45s	−69°12′47.3″	11.56	2.64E-17	2.E-18	1.91E-16	2.E-18
Arp 182	NGC 7674	23h27m56.71s	+08°46′44.3″	11.55	1.30E-14	1.E-16	9.96E-15	4.E-17
Arp 182	NGC 7674A	23h27m58.77s	+08°46′57.9″	10.01	1.23E-15	1.E-17	1.64E-15	6.E-18
GOALS J2341454-033944	MRK 933	23h41m43.69s	−03°39′26.5″	10.17	3.02E-15	6.E-17	2.88E-15	9.E-17
GOALS J2341454-033944	MCG-01-60-021	23h41m47.33s	−03°40′01.7″	10.43	3.58E-16	3.E-17
GOALS J2341454-033944	MCG-01-60-022	23h42m00.91s	−03°36′54.4″	11.15	7.99E-15	1.E-16	6.20E-15	2.E-16
KTG 82	NGC 7769	23h51m03.91s	+20°09′01.7″	10.74	3.39E-14	8.E-17	2.35E-14	6.E-17
KTG 82	NGC 7770	23h51m22.55s	+20°05′49.2″	10.67	1.07E-14	4.E-17	7.63E-15	3.E-17
KTG 82	NGC 7771	23h51m24.80s	+20°06′42.2″	11.17	5.13E-15	3.E-17	6.39E-15	3.E-17

Note. — Column (1): System name. Column (2): Galaxy name. Column (3): The right ascension (J2000) of the IRAC 8 μm centroid in Mazzarella et al. (2010). Column (4): The declination (J2000) of the IRAC 8 μm centroid in Mazzarella et al. (2010). Column (5): The infrared luminosity in \log_{10} Solar units computed using the MIPS flux densities reported in Mazzarella et al. (2010) and the luminosity distances in Armus et al. (2009); see text for details. Column (6): GALEX FUV flux density in units of $\text{erg s}^{-1}\text{cm}^{-2}\text{\AA}^{-1}$. Column (7): GALEX FUV flux density uncertainty. Column (8): GALEX NUV flux density in units of $\text{erg s}^{-1}\text{cm}^{-2}\text{\AA}^{-1}$. Column (9): GALEX NUV flux density uncertainty.

Table 3. Derived Quantities - Integrated Systems

System	$\log(L_{\text{FUV}})$	$\beta(\text{GALEX})$	$\sigma_{\beta}(\text{GALEX})$	IRX	σ_{IRX}	Mass M_{\odot}	SFR $M_{\odot}\text{yr}^{-1}$	SSFR yr^{-1}	IR/UV
(1)	(2)	(3)	(4)	(5)	(6)	(7)	(8)	(9)	(10)
NGC 0023	9.39	0.409	0.016	1.724	0.003	1.59E+11	23.34	1.47E-10	19.2
NGC 0034	9.69	-0.907	0.078	1.799	0.013	1.10E+11	[55.25]	[5.04E-10]	31.2
Arp 256	10.22	-0.139	0.016	1.262	0.003	1.80E+11	57.11	3.18E-10	7.6
ESO 350-IG038	10.15	-1.281	0.009	1.128	0.001	4.63E+10	[37.02]	[7.99E-10]	7.2
NGC 0232	9.04	-0.265	0.224	2.404	0.037	1.94E+11	48.65	2.50E-10	108.7
MCG+12-02-001	7.90	-1.915	2.361	3.593	0.343	8.10E+10	54.49	6.73E-10	2348.3
NGC 0317B	8.82	1.421	0.339	2.367	0.060	1.16E+11	26.97	2.33E-10	63.0
IC 1623	10.33	-0.649	0.010	1.379	0.002	1.62E+11	[94.09]	[5.80E-10]	11.2
MCG-03-04-014	9.52	0.100	0.034	2.127	0.006	1.64E+11	78.53	4.80E-10	52.5
ESO 244-G012	9.53	-0.376	0.104	1.848	0.017	1.37E+11	42.66	3.11E-10	31.1
CGCG 436-030	9.71	0.721	0.023	1.974	0.004	7.12E+10	[85.87]	[1.21E-09]	31.3
IRAS F01364-1042	8.71	2.662	0.284	3.136	0.051	4.33E+10	122.61	2.83E-09	247.6
NGC 0695	9.63	0.764	0.029	2.053	0.005	2.01E+11	84.64	4.21E-10	37.1
UGC 01385	9.50	-0.560	0.090	1.546	0.015	6.05E+10	20.32	3.36E-10	16.2
NGC 0877	9.59	-0.118	0.015	1.512	0.002	1.61E+11	22.83	1.41E-10	13.5
MCG+05-06-036	9.33	1.029	0.192	2.316	0.034	2.88E+11	77.18	2.68E-10	63.0
NGC 0958	9.62	-0.249	0.021	1.581	0.004	2.79E+11	28.71	1.03E-10	16.3
NGC 1068	9.53	-0.194	0.005	1.865	0.001	1.44E+11	[44.29]	[3.07E-10]	30.9
UGC 02238	8.74	-0.233	0.134	2.591	0.022	8.71E+10	37.70	4.33E-10	166.2
NGC 1275	9.67	-0.147	0.007	1.593	0.001	4.29E+11	[32.78]	[7.65E-11]	16.4
NGC 1365	9.24	-0.203	0.012	1.760	0.002	1.44E+11	[17.83]	[1.24E-10]	24.4
IRAS F03359+1523	8.98	0.660	0.873	2.562	0.157	5.56E+10	61.22	1.10E-09	123.2
CGCG 465-012	8.14	3.748	2.176	3.054	0.395	1.17E+11	27.51	2.35E-10	139.2
UGC 02982	8.06	-1.453	2.293	3.141	0.363	8.57E+10	27.71	3.23E-10	764.9
ESO 550-IG025	9.36	0.107	0.240	2.142	0.041	1.14E+11	56.46	4.95E-10	54.3
ESO 203-IG001	9.26	-0.195	0.112	2.606	0.019	7.33E+10	127.43	1.74E-09	170.5
MCG-05-12-006	8.69	2.091	0.388	2.479	0.069	4.39E+10	26.06	5.93E-10	65.9
CGCG 468-002	8.32	-0.940	1.609	2.900	0.269	8.37E+10	[29.15]	[3.48E-10]	396.5
IRAS05083+2441	7.95	1.277	2.568	3.313	0.460	7.86E+10	31.95	4.06E-10	581.5
IRAS05129+5128	8.54	0.244	1.422	2.882	0.248	5.07E+10	45.90	9.05E-10	288.1
IRAS F05189-2524	9.38	-0.362	0.130	2.783	0.022	3.19E+11	[253.48]	[7.95E-10]	266.5
NGC 1961	9.66	-0.146	0.011	1.403	0.002	3.92E+11	21.38	5.45E-11	10.6
UGC 03410	8.72	-0.199	0.218	2.383	0.037	1.23E+11	22.03	1.79E-10	102.0
NGC 2146	8.30	0.789	0.025	2.820	0.004	6.41E+10	22.87	3.57E-10	215.2
ESO 255-IG007	9.85	-0.110	0.030	2.048	0.005	1.80E+11	140.00	7.79E-10	46.1
NGC 2342	9.86	-0.274	0.063	1.453	0.011	1.97E+11	37.60	1.90E-10	12.2
NGC 2369	8.73	-0.199	0.213	2.427	0.036	1.24E+11	25.00	2.01E-10	113.0
NGC 2388	9.72	-0.721	0.015	1.559	0.002	1.43E+11	34.74	2.43E-10	17.3
MCG+02-20-003	9.45	-0.563	0.096	1.680	0.016	8.22E+10	[24.22]	[2.95E-10]	22.0
NGC 2623	9.25	-0.234	0.038	2.351	0.006	6.42E+10	69.19	1.08E-09	95.6
ESO 060-IG016	9.32	0.945	0.238	2.495	0.042	9.37E+10	[115.40]	[1.23E-09]	97.5
IRAS F08572+3915	9.62	0.791	0.103	2.548	0.018	6.38E+11	[254.32]	[3.98E-10]	115.1
IRAS 09022-3615	8.86	3.672	0.650	3.451	0.118	1.66E+11	[359.05]	[2.17E-09]	356.6
IRAS F09111-1007	9.44	1.304	0.106	2.619	0.019	1.43E+11	198.46	1.39E-09	116.8
UGC 04881	9.55	0.726	0.040	2.197	0.007	2.59E+11	97.13	3.76E-10	52.3
UGC 05101	9.09	0.876	0.136	2.925	0.024	1.97E+11	[180.18]	[9.15E-10]	267.6
MCG+08-18-013	9.78	-0.974	0.100	1.555	0.016	7.42E+10	39.55	5.33E-10	18.1
Arp 303	9.26	-0.220	0.153	1.968	0.026	1.73E+11	29.83	1.72E-10	39.5
NGC 3110	9.72	-0.183	0.085	1.646	0.014	1.32E+11	41.72	3.15E-10	18.6
ESO 374-IG032	9.39	2.969	0.054	2.394	0.010	2.89E+11	[106.13]	[3.67E-10]	40.3
IRAS F10173+0828	7.10	12.181	11.648	4.760	2.118	3.67E+10	126.32	3.44E-09	235.0
NGC 3221	9.19	0.169	0.119	1.896	0.020	1.55E+11	21.75	1.40E-10	30.3
NGC 3256	9.34	0.433	0.018	2.299	0.003	1.14E+11	76.46	6.71E-10	71.6
ESO 264-G036	7.54	8.485	12.042	3.781	2.189	2.45E+11	36.54	1.49E-10	114.3
IRAS F10565+2448	8.83	1.997	0.237	3.247	0.042	1.49E+11	209.13	1.40E-09	398.4
MCG+07-23-019	9.86	-0.804	0.111	1.761	0.020	9.36E+10	75.13	8.03E-10	28.0
CGCG 011-076	8.56	1.114	0.517	2.871	0.090	1.31E+11	46.52	3.55E-10	220.4
IRAS F11231+1456	9.23	0.897	0.240	2.413	0.041	1.84E+11	76.35	4.15E-10	81.8
NGC 3690	10.16	-0.923	0.029	1.771	0.005	1.55E+11	[150.55]	[9.74E-10]	29.4
ESO 320-G030	8.47	0.633	0.255	2.693	0.045	4.63E+10	25.64	5.54E-10	168.0
ESO 440-IG058	9.11	1.027	0.336	2.325	0.059	1.24E+11	47.53	3.83E-10	64.4
IRAS F12112+0305	9.85	-0.606	0.064	2.510	0.010	2.17E+11	402.89	1.85E-09	150.4
ESO 267-G030	8.99	-0.060	0.473	2.260	0.082	2.57E+11	31.31	1.22E-10	74.4
NGC 4922	8.89	1.073	0.080	2.489	0.014	1.73E+11	[41.95]	[2.42E-10]	92.6
CGCG 043-099	9.36	-0.516	0.299	2.330	0.048	1.19E+11	84.73	7.11E-10	97.2

Table 3—Continued

System	$\log(L_{\text{FUV}})$	$\beta(\text{GALEX})$	$\sigma_{\beta}(\text{GALEX})$	IRX	σ_{IRX}	Mass M_{\odot}	SFR $M_{\odot}\text{yr}^{-1}$	SSFR yr^{-1}	IR/UV
(1)	(2)	(3)	(4)	(5)	(6)	(7)	(8)	(9)	(10)
MCG-02-33-098-9	9.19	0.612	0.161	1.973	0.028	5.91E+10	25.87	4.38E-10	32.2
ESO 507-G070	9.01	-0.040	0.115	2.544	0.020	1.23E+11	62.77	5.12E-10	142.1
VV 250a	9.89	0.057	0.111	1.913	0.019	1.12E+11	113.75	1.01E-09	32.4
UGC 08387	9.35	0.284	0.156	2.379	0.026	6.72E+10	94.18	1.40E-09	89.6
NGC 5104	9.05	-0.060	0.210	2.220	0.035	1.36E+11	32.52	2.38E-10	67.7
MCG-03-34-064	8.99	0.022	0.488	2.204	0.042	1.19E+11	[27.08]	[2.27E-10]	63.7
NGC 5135	9.49	0.195	0.084	1.804	0.014	1.27E+11	[35.41]	[2.79E-10]	24.4
IC 4280	9.49	0.391	0.109	1.661	0.019	1.45E+11	25.24	1.74E-10	16.7
NGC 5256	9.88	-0.176	0.107	1.679	0.018	1.66E+11	65.00	3.92E-10	20.1
Arp 240	10.32	-0.592	0.043	1.292	0.007	3.02E+11	77.47	2.57E-10	9.1
UGC 08739	9.29	-0.730	0.183	1.854	0.030	9.89E+10	24.99	2.53E-10	34.1
NGC 5331	9.75	0.011	0.029	1.911	0.005	2.66E+11	80.41	3.02E-10	32.7
Arp 84	9.08	0.398	0.118	1.993	0.021	2.11E+11	20.99	9.94E-11	35.7
CGCG 247-020	8.48	-0.627	1.038	2.911	0.167	5.54E+10	42.81	7.72E-10	380.3
NGC 5653	9.49	0.017	0.077	1.640	0.013	1.03E+11	24.24	2.36E-10	17.5
IRAS F14348-1447	9.92	-0.792	0.138	2.466	0.023	3.74E+11	428.54	1.14E-09	141.6
NGC 5734	9.34	-0.237	0.103	1.813	0.017	1.89E+11	25.25	1.33E-10	27.7
VV 340a	9.80	-0.376	0.026	1.950	0.046	3.15E+11	98.31	3.12E-10	39.3
CGCG 049-057	7.20	5.900	5.898	4.156	1.072	1.97E+10	39.16	1.99E-09	770.7
VV 705	9.86	-0.559	0.152	2.061	0.025	1.56E+11	147.81	9.48E-10	52.9
IRAS F15250+3608	9.82	-0.169	0.191	2.264	0.034	6.08E+10	211.11	3.47E-09	77.0
NGC 5936	9.69	-0.398	0.064	1.450	0.011	9.68E+10	25.23	2.61E-10	12.5
UGC 09913	8.85	0.997	0.329	3.423	0.038	1.16E+11	327.74	2.82E-09	813.3
NGC 5990	9.32	-0.190	0.106	1.817	0.018	1.42E+11	[24.19]	[1.70E-10]	27.7
NGC 6052	10.01	-0.755	0.050	1.080	0.009	4.76E+10	24.09	5.06E-10	5.8
NGC 6090	10.26	-0.176	0.017	1.325	0.003	2.24E+11	71.10	3.17E-10	8.9
IRAS F16164-0746	9.05	-0.431	0.161	2.573	0.028	7.34E+10	72.75	9.91E-10	167.0
CGCG 052-037	8.97	0.430	0.352	2.475	0.061	1.18E+11	48.75	4.13E-10	107.3
NGC 6240	9.59	0.003	0.168	2.336	0.031	3.90E+11	[148.44]	[3.81E-10]	87.1
NGC 6286	9.39	-0.298	0.114	1.976	0.019	1.64E+11	41.26	2.51E-10	41.0
IRAS F17132+5313	9.53	0.364	0.073	2.435	0.013	1.72E+11	159.67	9.28E-10	99.8
IRAS F17207-0014	7.31	4.576	8.665	5.154	1.574	1.52E+11	501.22	3.29E-09	12840.8
UGC 11041	9.11	-0.559	0.174	2.000	0.029	7.92E+10	22.85	2.89E-10	45.9
CGCG 141-034	8.60	-1.561	0.773	2.597	0.117	5.60E+10	27.39	4.89E-10	222.8
NGC 6621	9.36	0.203	0.126	1.930	0.021	1.55E+11	34.28	2.21E-10	32.5
IC 4687	9.73	-0.465	0.065	1.895	0.011	1.60E+11	74.70	4.66E-10	35.3
NGC 6670AB	9.36	0.177	0.049	2.290	0.008	1.90E+11	78.26	4.12E-10	74.9
IC 4734	9.30	-0.696	0.141	2.045	0.023	9.10E+10	39.30	4.32E-10	52.6
ESO 593-IG008	9.72	1.894	0.439	2.209	0.080	3.53E+11	150.38	4.26E-10	42.9
IRAS F19297-0406	8.05	0.433	1.073	4.401	0.179	1.72E+11	494.79	2.88E-09	9041.1
ESO 339-G011	8.88	0.764	0.380	2.322	0.066	1.03E+11	[27.62]	[2.69E-10]	68.9
NGC 6907	9.98	-0.622	0.009	1.134	0.001	1.54E+11	25.24	1.64E-10	6.3
NGC 6926	9.71	-0.757	0.090	1.609	0.015	1.95E+11	[37.50]	[1.92E-10]	19.5
CGCG 448-020	10.28	-1.134	0.099	1.662	0.016	1.34E+11	156.77	1.17E-09	23.9
ESO 286-IG019	9.95	-0.206	0.027	2.108	0.005	1.13E+11	203.56	1.80E-09	54.3
ESO 286-G035	9.09	0.196	0.176	2.102	0.030	5.84E+10	27.58	4.72E-10	48.4
ESO 343-IG013	9.12	0.173	0.214	2.014	0.036	6.75E+10	24.22	3.59E-10	39.8
NGC 7130	9.71	0.327	0.017	1.712	0.003	1.45E+11	[46.88]	[3.23E-10]	19.1
IC 5179	9.62	-0.137	0.058	1.619	0.010	1.23E+11	31.01	2.52E-10	17.3
ESO 602-G025	9.30	-0.169	0.264	2.037	0.044	1.37E+11	38.38	2.80E-10	45.6
UGC 12150	7.59	5.341	5.742	3.760	1.043	1.10E+11	38.87	3.55E-10	386.2
IRAS F22491-1808	10.00	0.176	0.076	2.198	0.013	2.27E+11	279.16	1.23E-09	60.7
NGC 7469	10.02	-0.748	0.008	1.632	0.001	2.39E+11	[80.26]	[3.35E-10]	20.6
CGCG 453-062	8.61	1.285	0.659	2.768	0.116	8.99E+10	41.52	4.62E-10	165.3
ESO 148-IG002	10.01	-0.282	0.025	2.054	0.004	1.06E+11	204.60	1.94E-09	48.8
IC 5298	9.15	-0.553	0.312	2.451	0.051	1.29E+11	69.67	5.38E-10	129.7
NGC 7552	9.32	0.403	0.005	1.793	0.001	7.62E+10	[22.98]	[3.01E-10]	22.5
NGC 7592	10.07	-1.240	0.067	1.332	0.011	1.13E+11	[47.03]	[4.15E-10]	11.4
ESO 077-IG014	8.90	1.576	0.211	2.856	0.038	1.77E+11	100.48	5.68E-10	185.3
NGC 7674	10.00	-0.489	0.022	1.560	0.004	3.03E+11	[65.76]	[2.17E-10]	16.4
IRAS F23365+3604	9.33	3.515	0.183	2.872	0.033	1.41E+11	276.72	1.96E-09	99.8
MCG-01-60-022	9.52	-0.671	0.031	1.752	0.005	2.08E+11	33.35	1.61E-10	26.6
Arp 86	9.40	-0.263	0.030	1.667	0.005	2.84E+11	21.21	7.47E-11	19.9
NGC 7771	9.78	-0.880	0.006	1.621	0.001	4.00E+11	45.12	1.13E-10	20.6
MRK0331	8.92	0.129	0.094	2.575	0.016	8.23E+10	55.14	6.70E-10	146.4

Table 3—Continued

System	$\log(L_{\text{FUV}})$	$\beta(\text{GALEX})$	$\sigma_{\beta}(\text{GALEX})$	IRX	σ_{IRX}	Mass M_{\odot}	SFR $M_{\odot}\text{yr}^{-1}$	SSFR yr^{-1}	IR/UV
(1)	(2)	(3)	(4)	(5)	(6)	(7)	(8)	(9)	(10)

Note. — Column (1): System name. Column (2): The total FUV luminosity in \log_{10} Solar units. Column (3): $\beta(\text{GALEX})$ calculated as described in §3.1, Equation 1. Column (4): $\beta(\text{GALEX})$ uncertainty. Column (5): Ratio of IR to FUV flux IRX calculated as described in §3.1. Column (6): IRX uncertainty. Column (7): Stellar mass calculated as described in §3.2. Column (8): Star formation rate calculated as described in §3.2. Values in brackets should be considered upper limits due to possible AGN contamination. Column (9): Specific star formation rate calculated as described in §3.2. Values in brackets should be considered upper limits due to possible AGN contamination. Column (10): IR/UV ratio calculated as described in §3.2, Equation 2.

Table 4. Derived Quantities - Resolved Components

Galaxy	$\log(L_{\text{FUV}})$	$\beta(\text{GALEX})$	$\sigma_{\beta}(\text{GALEX})$	IRX	σ_{IRX}	Mass M_{\odot}	SFR $M_{\odot}\text{yr}^{-1}$	SSFR yr^{-1}
(1)	(2)	(3)	(4)	(5)	(6)	(7)	(8)	(9)
NGC 0034	9.69	-0.91	0.15	1.739	0.013	8.92E+10	[46.91]	[5.26E-10]
NGC 0035	9.35	0.53	0.19	1.257	0.020	2.05E+10	6.99	3.41E-10
MCG-02-01-052	9.89	-0.39	0.03	0.468	0.004	...	3.95	...
MCG-02-01-051	9.95	-0.64	0.03	1.501	0.003	...	48.63	...
NGC 0232	9.04	-0.26	0.55	2.312	0.037	1.10E+11	39.14	3.57E-10
NGC 0235A	8.73	-0.18	1.05	1.998	0.062	8.46E+10	[9.21]	[1.09E-10]
NGC 0317A	7.84	4.09	0.34	1.120	0.060	8.15E+10	0.16	1.95E-12
NGC 0317B	8.77	0.76	0.34	2.412	0.060	3.44E+10	26.63	7.73E-10
IC 1623A	10.31	-0.71	0.01	0.773	0.002	1.37E+11	21.07	1.54E-10
IC 1623B	8.88	0.65	0.01	2.703	0.002	4.72E+10	[67.19]	[1.42E-09]
ESO 244-G012 NED01	9.45	-0.62	0.10	0.042	0.017	...	0.53	...
ESO 244-G012 NED02	8.79	0.49	0.10	2.584	0.017	...	41.19	...
UGC 01385	8.75	-0.28	0.48	2.271	0.040	4.74E+10	18.30	3.86E-10
KUG 0152+366	9.42	-0.62	0.16	0.399	0.016	1.31E+10	1.14	8.71E-11
NGC 0876	9.59	-0.12	0.02	0.923	0.002	2.43E+10	5.60	2.31E-10
NGC 0877	8.24	0.06	0.32	2.727	0.021	1.37E+11	16.17	1.18E-10
MCG+05-06-035	9.17	1.09	0.19	1.980	0.034	1.89E+11	24.84	1.31E-10
MCG+05-06-036	8.80	0.88	0.19	2.672	0.034	9.86E+10	51.76	5.25E-10
UGC 02894	8.80	-0.34	1.31	1.827	0.093	4.73E+10	7.28	1.54E-10
CGCG 465-012	8.15	3.75	2.38	2.920	0.395	6.95E+10	20.18	2.90E-10
ESO 550-IG025 NED01	9.28	-0.01	0.24	1.994	0.041	...	32.28	...
ESO 550-IG025 NED02	8.64	0.55	0.24	2.497	0.041	...	23.54	...
CGCG 468-002 NED01	7.07	4.40	1.61	3.669	0.269	6.54E+10	9.57	1.46E-10
CGCG 468-002 NED02	8.30	-2.57	1.61	2.751	0.269	1.83E+10	[19.52]	[1.06E-09]
IRAS 05083+2441	7.95	1.10	3.94	3.264	0.462	5.56E+10	28.38	5.11E-10
2MASX J05112888+2445593	5.66	7.79	483.06	4.650	87.595	2.30E+10	3.54	1.54E-10
UGC 03405	8.72	-0.20	0.46	1.626	0.037	3.73E+10	3.83	1.03E-10
UGC 03410	8.23	0.19	1.18	2.787	0.096	8.55E+10	18.05	2.11E-10
NGC 2341	9.15	0.80	0.31	1.830	0.032	7.10E+10	16.69	2.35E-10
NGC 2342	9.86	-0.27	0.11	1.178	0.011	1.27E+11	18.93	1.50E-10
NGC 2385	7.76	4.19	0.48	1.923	0.079	2.76E+10	0.84	3.04E-11
NGC 2388	9.72	-0.72	0.03	1.453	0.002	7.73E+10	26.11	3.38E-10
NGC 2389	7.11	3.86	2.12	3.453	0.334	3.83E+10	6.34	1.65E-10
NGC 2416	9.45	-0.56	0.20	3.30E+10
MCG+02-20-003	9.14	0.73	0.25	4.92E+10
2MASX J09133644-1019296	7.90	2.62	1.02	4.049	0.181	...	154.77	...
2MASX J09133888-1019196	9.45	1.10	0.06	1.942	0.010	...	42.94	...
UGC 04881 NED02	7.98	0.82	0.22	3.285	0.038	8.52E+10	32.23	3.78E-10
UGC 04881 NED01	8.37	0.78	0.13	3.192	0.023	1.73E+11	63.94	3.69E-10
CGCG 239-011 NED01	9.63	-1.39	0.23	0.345	0.020	6.25E+09	1.65	2.64E-10
MCG+08-18-013	9.25	-0.19	0.32	2.066	0.032	6.79E+10	36.24	5.34E-10
2MASX J11210825-0259399	8.26	-0.51	2.74	2.127	0.154	9.64E+09	4.23	4.39E-10
CGCG 011-076	8.25	2.09	1.27	3.134	0.157	1.21E+11	42.19	3.48E-10
IC 2810A	9.19	0.93	0.40	2.266	0.044	1.21E+11	49.68	4.09E-10
IC 2810B	8.14	0.56	3.82	3.035	0.253	6.26E+10	26.21	4.19E-10
NGC 3690	10.00	-0.87	0.03	1.766	0.005	1.26E+11	[101.44]	[8.02E-10]
IC 0694	9.63	-1.06	0.03	1.780	0.005	7.79E+10	[45.19]	[5.80E-10]
ESO 440-IG058 NED01	8.97	0.95	0.34	1.574	0.059	...	6.02	...
ESO 440-IG058 NED02	8.56	1.20	0.34	2.819	0.059	...	41.15	...
ESO 267-G029	9.39	-0.70	0.52	1.537	0.037	9.56E+10	14.52	1.52E-10
ESO 267-G030	8.99	-0.06	1.00	1.986	0.082	1.61E+11	16.52	1.03E-10
NGC 4922 NED01	8.30	2.02	0.08	0.576	0.014	...	0.13	...
NGC 4922 NED02	8.76	0.64	0.08	2.615	0.014	...	[41.61]	...
MCG-02-33-098	8.60	2.00	0.16	2.406	0.028	...	17.52	...
MCG-02-33-099	9.07	-0.13	0.16	1.593	0.028	...	7.93	...
VV 250b	9.42	-0.10	0.11	4.60E+10
VV 250a	9.72	0.13	0.11	6.62E+10
MRK 266B	9.51	-0.22	0.11	1.853	0.018	...	40.44	...
MRK 266A	9.64	-0.15	0.11	1.477	0.018	...	22.48	...
NGC 5257	9.77	-0.33	0.13	1.541	0.014	1.42E+11	35.66	2.50E-10
NGC 5258	10.18	-0.70	0.08	1.136	0.009	1.59E+11	36.03	2.26E-10
NGC 5331 NED01	9.15	0.45	0.03	2.393	0.005	...	60.78	...
NGC 5331 NED02	9.62	-0.16	0.03	1.398	0.005	...	18.10	...
NGC 5734	8.73	1.01	0.48	2.204	0.051	1.23E+11	15.09	1.23E-10
NGC 5743	9.34	-0.24	0.20	1.401	0.017	6.63E+10	9.56	1.44E-10

Table 4—Continued

Galaxy	$\log(L_{\text{FUV}})$	$\beta(\text{GALEX})$	$\sigma_{\beta}(\text{GALEX})$	IRX	σ_{IRX}	Mass M_{\odot}	SFR $M_{\odot}\text{yr}^{-1}$	SSFR yr^{-1}
(1)	(2)	(3)	(4)	(5)	(6)	(7)	(8)	(9)
VV 340b	9.58	-0.39	0.03	1.425	0.005	6.86E+10	17.56	2.56E-10
VV 340a	9.05	-0.44	0.06	2.610	0.010	2.46E+11	79.04	3.21E-10
NGC 6285	9.11	-0.22	0.25	1.532	0.026	3.84E+10	7.58	1.97E-10
NGC 6286	9.07	-0.39	0.28	2.204	0.027	1.26E+11	33.01	2.63E-10
NGC 6621	8.87	1.09	0.13	2.401	0.021	...	32.78	...
NGC 6621 SE	9.17	-0.69	0.13	0.355	0.021	...	0.58	...
NGC 6622	7.78	2.81	0.13	1.451	0.021	...	0.29	...
IC 4686	9.54	-0.12	0.07	1.499	0.012	2.28E+10	19.22	8.41E-10
IC 4687	9.10	-0.38	0.07	2.241	0.012	8.69E+10	38.51	4.43E-10
IC 4689	8.77	-0.57	0.62	2.176	0.045	5.04E+10	15.49	3.07E-10
NGC 6670B	8.77	0.27	0.08	2.558	0.014	1.25E+11	36.78	2.95E-10
NGC 6670A	9.14	-0.17	0.05	2.229	0.008	6.53E+10	41.39	6.34E-10
ESO 343-IG013 NED01	8.95	0.12	0.21	1.649	0.036	...	6.85	...
ESO 343-IG013 NED02	8.65	0.28	0.21	2.342	0.036	...	17.01	...
NGC 7469	10.00	-0.78	0.01	1.585	0.001	1.95E+11	[66.69]	[3.41E-10]
IC 5283	8.61	-0.02	0.08	2.179	0.007	4.39E+10	10.72	2.44E-10
NGC 7592A	9.08	-0.83	0.07	2.097	0.011	...	[25.85]	...
NGC 7592B	10.02	-1.29	0.07	0.991	0.011	...	17.96	...
ESO 077-IG014 NED01	8.88	1.21	0.21	2.448	0.038	1.23E+11	37.28	3.04E-10
ESO 077-IG014 NED02	7.60	4.73	0.21	3.960	0.038	5.42E+10	62.98	1.16E-09
NGC 7674	9.96	-0.64	0.02	1.587	0.004	2.49E+11	[61.26]	[2.46E-10]
NGC 7674A	8.94	0.69	0.02	1.072	0.004	5.37E+10	1.77	3.29E-11
MRK 933	9.14	-0.11	0.09	0.772	0.008	6.43E+09	1.41	2.19E-10
MCG-01-60-021	8.21	1.963	0.035	1.30E+11	2.59	2.00E-11
MCG-01-60-022	9.56	-0.61	0.07	1.654	0.005	7.16E+10	28.44	3.97E-10
NGC 7769	9.78	-0.88	0.01	0.961	0.001	1.38E+11	9.53	6.90E-11
NGC 7770	9.28	-0.80	0.01	1.396	0.002	2.59E+10	[8.16]	[3.15E-10]
NGC 7771	8.96	0.52	0.02	2.214	0.003	2.37E+11	25.79	1.09E-10

Note. — Column (1): Galaxy name. Column (2): The total FUV luminosity in \log_{10} Solar units. Column (3): $\beta(\text{GALEX})$ calculated as described in §3.1, Equation 1. Column (4): $\beta(\text{GALEX})$ uncertainty. Column (5): Ratio of IR to FUV flux IRX calculated as described in §3.1. Column (6): IRX uncertainty. Column (7): Stellar mass calculated as described in §3.2. Column (8): Star formation rate calculated as described in §3.2. Values in brackets should be considered upper limits due to possible AGN contamination. Column (9): Specific star formation rate calculated as described in §3.2. Values in brackets should be considered upper limits due to possible AGN contamination.

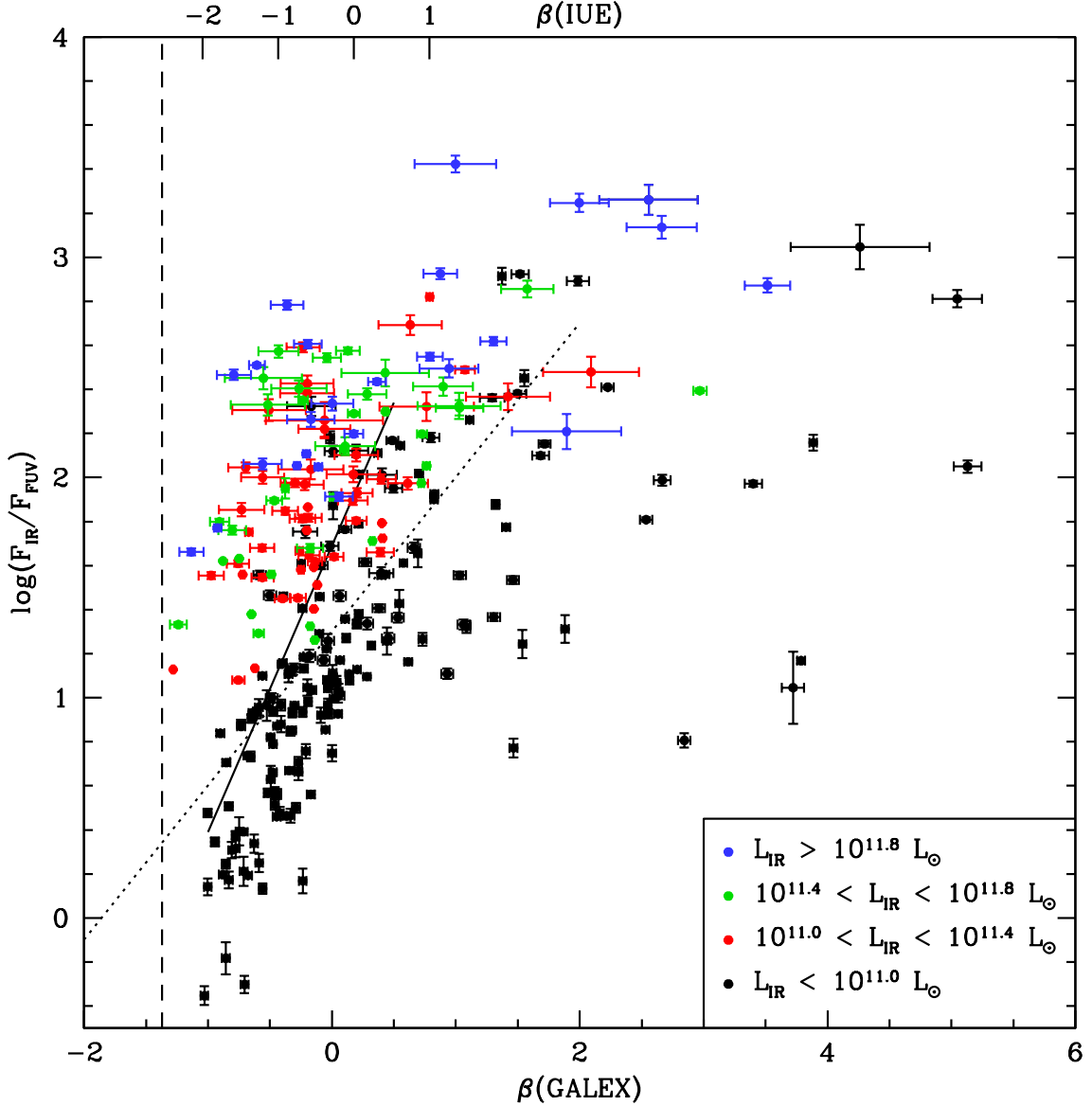


Fig. 1.— The IR excess, $F_{\text{IR}}/F_{\text{FUV}}$, plotted against the UV continuum slope, $\beta(\text{GALEX})$. Black points (from GDP) have $L_{\text{IR}} < 10^{11} L_{\odot}$, red points have $10^{11} < L_{\text{IR}} < 10^{11.4} L_{\odot}$, green points have $10^{11.4} < L_{\text{IR}} < 10^{11.8} L_{\odot}$, and blue points have $L_{\text{IR}} > 10^{11.8} L_{\odot}$. The solid line is a fit to the starburst galaxies of Meurer et al. (1999) which were included in the GDP sample. The dotted line is the fit to the late-type galaxy sample of Cortese et al. (2006). The vertical dashed line is the UV color of a Starburst99 (Leitherer et al. 1999) model of a 10^8 year old starburst population with solar metallicity and a Salpeter IMF (Salpeter 1955). The range of $\beta(\text{GALEX})$ in the IUE system of Meurer et al. (1999) is shown at top. Low and medium luminosity LIRGs (red and green points) fill parameter space between normal galaxies and high luminosity LIRGs and ULIRGs (blue points).

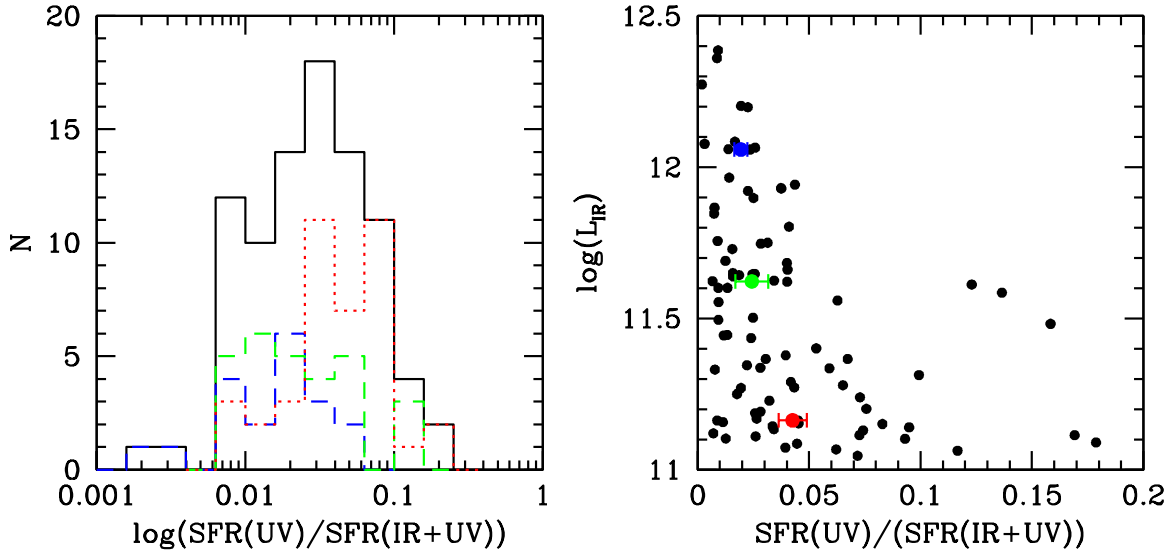


Fig. 2.— Left: Histogram showing the ratio of SFR(UV) to SFR(UV+IR). The solid line is the full GOALS GALEX sample. Colored lines show the GOALS GALEX sample divided into luminosity bins as in Fig. 1: $10^{11} < L_{\text{IR}} < 10^{11.4} L_{\odot}$ (red dotted line), $10^{11.4} < L_{\text{IR}} < 10^{11.8} L_{\odot}$ (green dashed line), and $L_{\text{IR}} > 10^{11.8} L_{\odot}$ (blue dashed line). The FUV contribution to SFR is small for (U)LIRGs and decreases with increasing L_{IR} . Right: L_{IR} plotted against the ratio of SFR(UV) to SFR(UV+IR). Median ratios of the star formation rates are shown for each luminosity bin (red: $10^{11} < L_{\text{IR}} < 10^{11.4} L_{\odot}$, green: $10^{11.4} < L_{\text{IR}} < 10^{11.8} L_{\odot}$, blue: $L_{\text{IR}} > 10^{11.8} L_{\odot}$) along with 1σ standard deviations of the mean. Although anticorrelated (Spearman rank correlation coefficient of -0.47) the correlation is not linear.

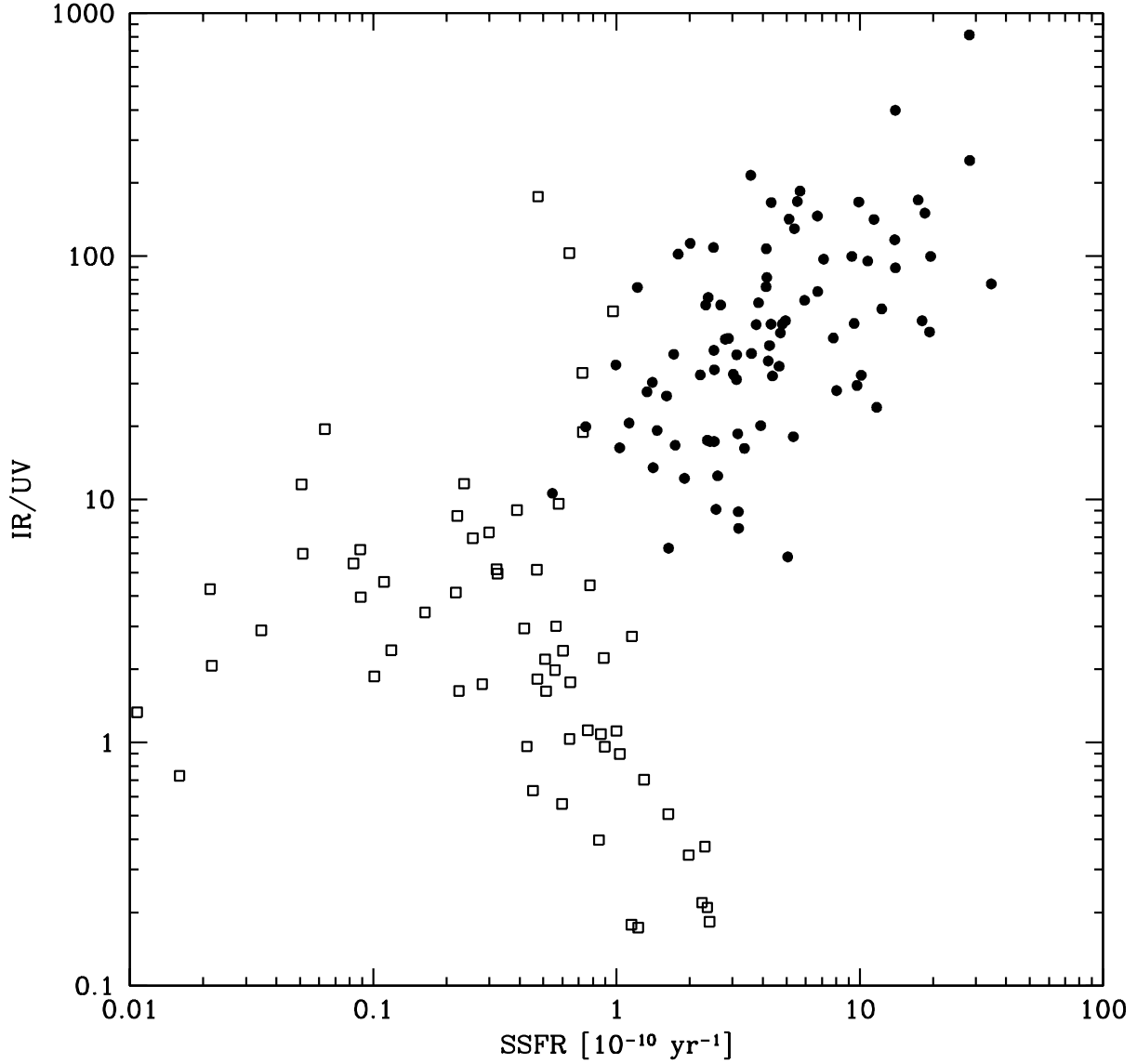


Fig. 3.— The IR/UV ratio plotted against specific star formation rate. Solid circles are GOALS galaxies (not including those with IRAC colors suggesting a strong AGN), while open squares are SINGS galaxies (Dale et al. 2007). The GOALS outlier at the high IR/UV, high SSFR extreme is Arp 220. LIRGs and ULIRGs have much higher IR/UV ratios and SSFR than lower luminosity galaxies, and the two quantities are correlated for GOALS systems and anti-correlated for SINGS galaxies with $\text{SSFR} > 10^{-11} \text{ yr}^{-1}$.

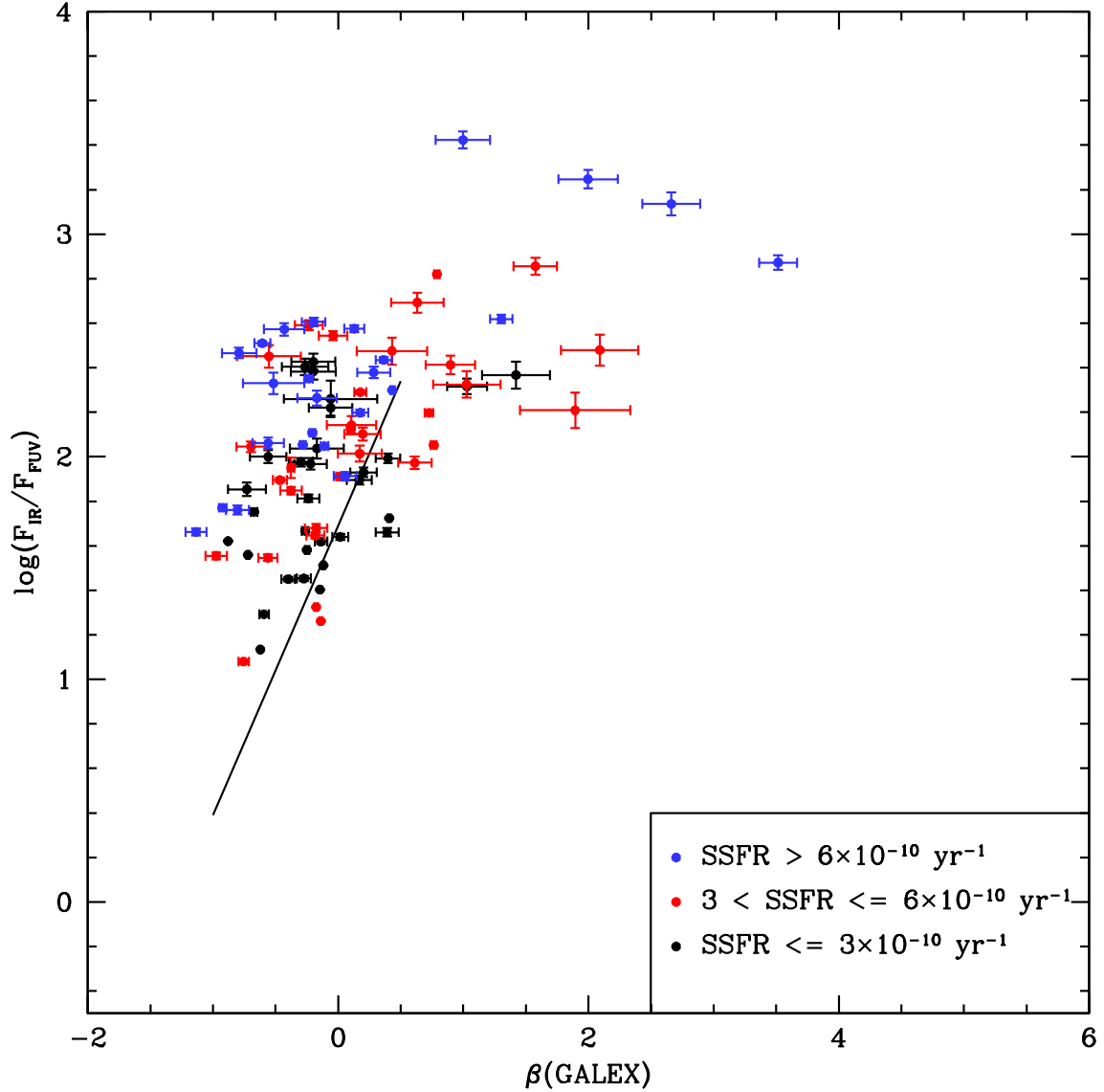


Fig. 4.— IRX- $\beta(\text{GALEX})$ plot with GOALS systems (not including those with IRAC colors suggesting a strong AGN) color-coded by specific SFR: black points have SSFR within the range spanned by SINGS galaxies, red points have up to twice the SSFR of any SINGS galaxy, and blue points have more than twice the SSFR of any SINGS galaxy. The solid line is the same as in Fig. 1. Systems with higher SSFR are systematically redder in β and have larger IRX than systems with lower SSFR.

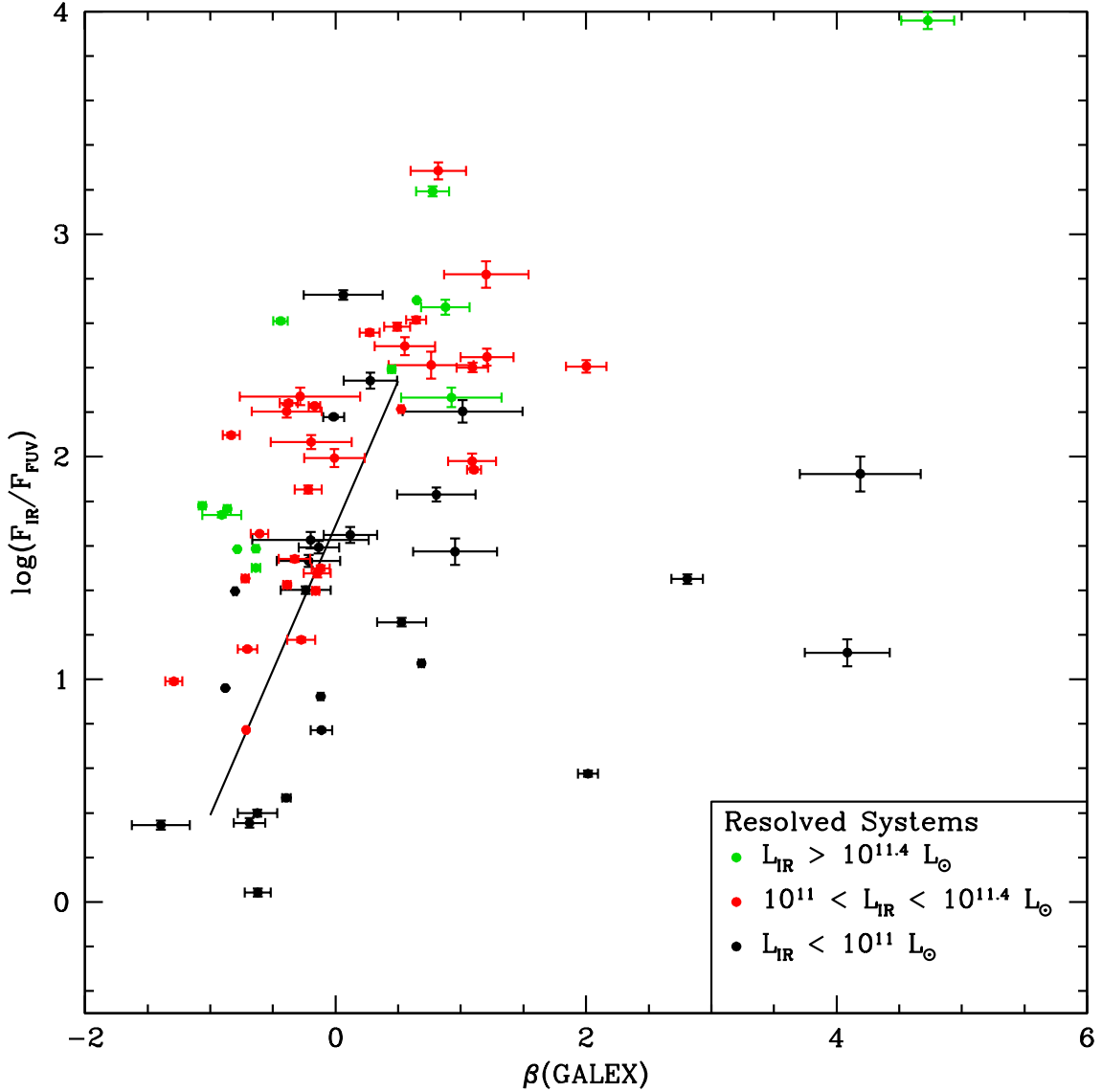


Fig. 5.— IRX- $\beta(\text{GALEX})$ plot showing the locations of individual galaxies in resolved pairs. As in Fig. 1, black points have $L_{\text{IR}} < 10^{11} L_{\odot}$, red points have $10^{11} < L_{\text{IR}} < 10^{11.4} L_{\odot}$, and green points have $10^{11.4} < L_{\text{IR}} < 10^{11.8} L_{\odot}$. The solid line is the same as in Fig. 1. Sub-LIRG galaxies are on average consistent with the GDP sample. LIRGs are on average offset above the starburst relation, with $L_{\text{IR}} > 10^{11.4} L_{\odot}$ systems having larger offsets than lower luminosity LIRGs.

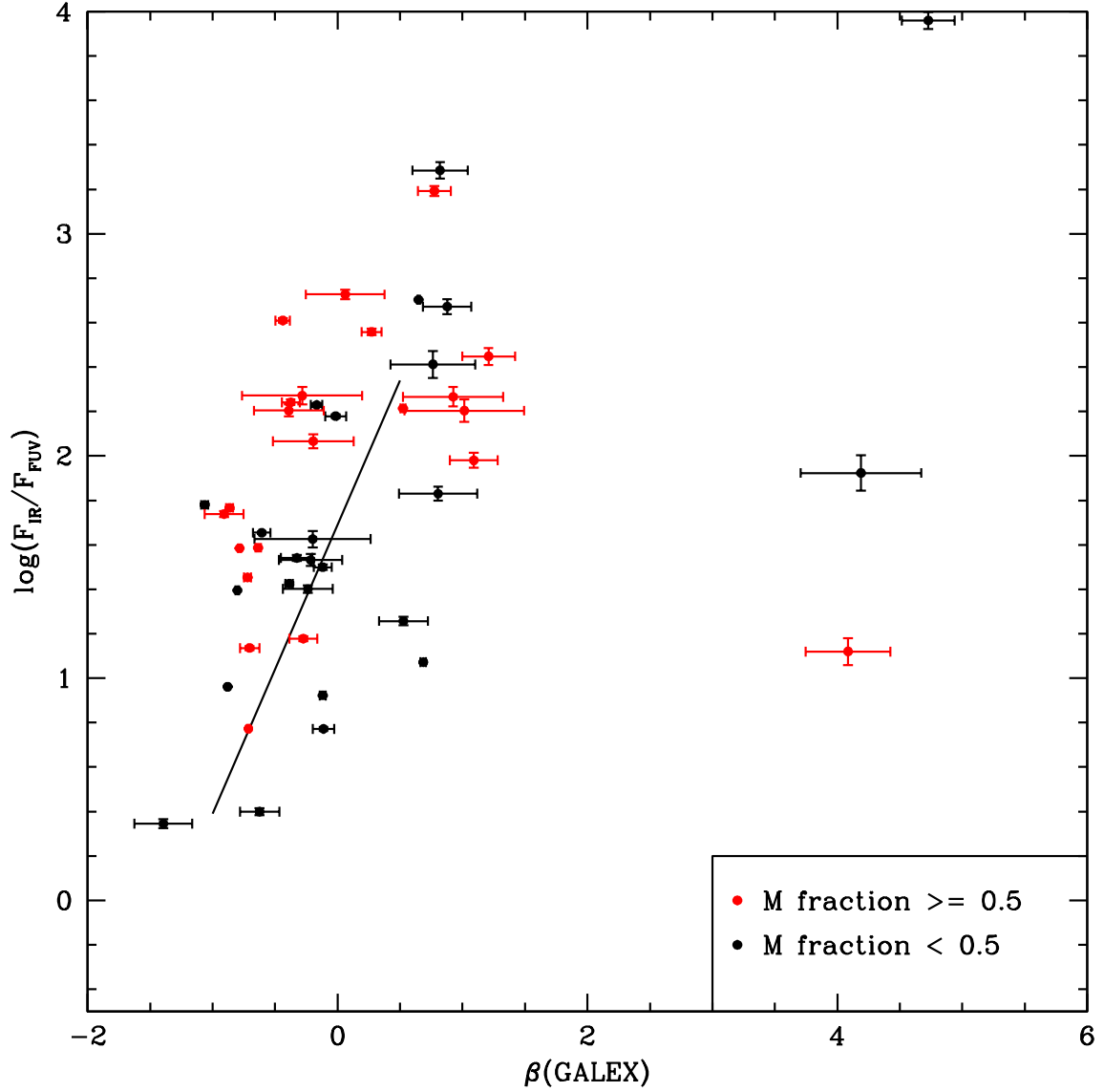


Fig. 6.— IRX- $\beta(\text{GALEX})$ plot showing the location of individual galaxies in close pairs for which a mass could be estimated. The galaxy with $> 50\%$ of the mass in each system is shown in red, while other galaxies are in black. The solid line shows the starburst relation, as in Fig. 1. On average, the high mass galaxy in a system is offset above the starburst relation, while the lower mass galaxy lies slightly below the starburst relation.

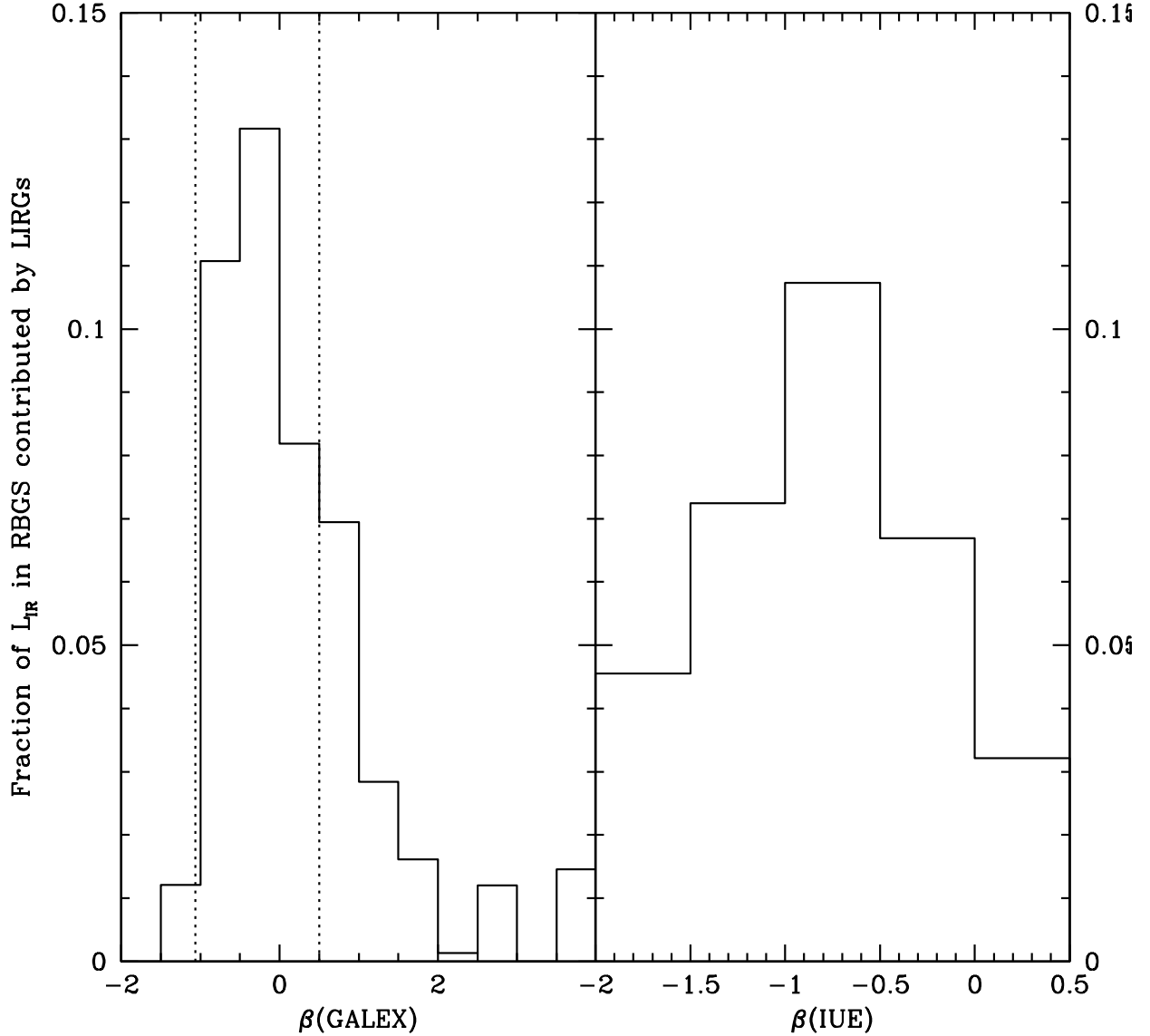


Fig. 7.— The fraction of total IR luminosity summed over all 629 systems in the RBGS sample contributed by LIRGs and ULIRGs with known UV colors (the GOALS GALEX sample, 112 systems). The IR luminosity fraction defined in this way is shown as a function of $\beta(\text{GALEX})$ (left panel) and $\beta(\text{IUE})$ (right panel) over the range of the conversion given in Appendix A. The dotted lines in the left panel mark the range of $\beta(\text{GALEX})$ shown in the right panel. At least 19% of the IR luminosity of the RBGS is produced by (U)LIRGs with red UV colors ($\beta > 0$).

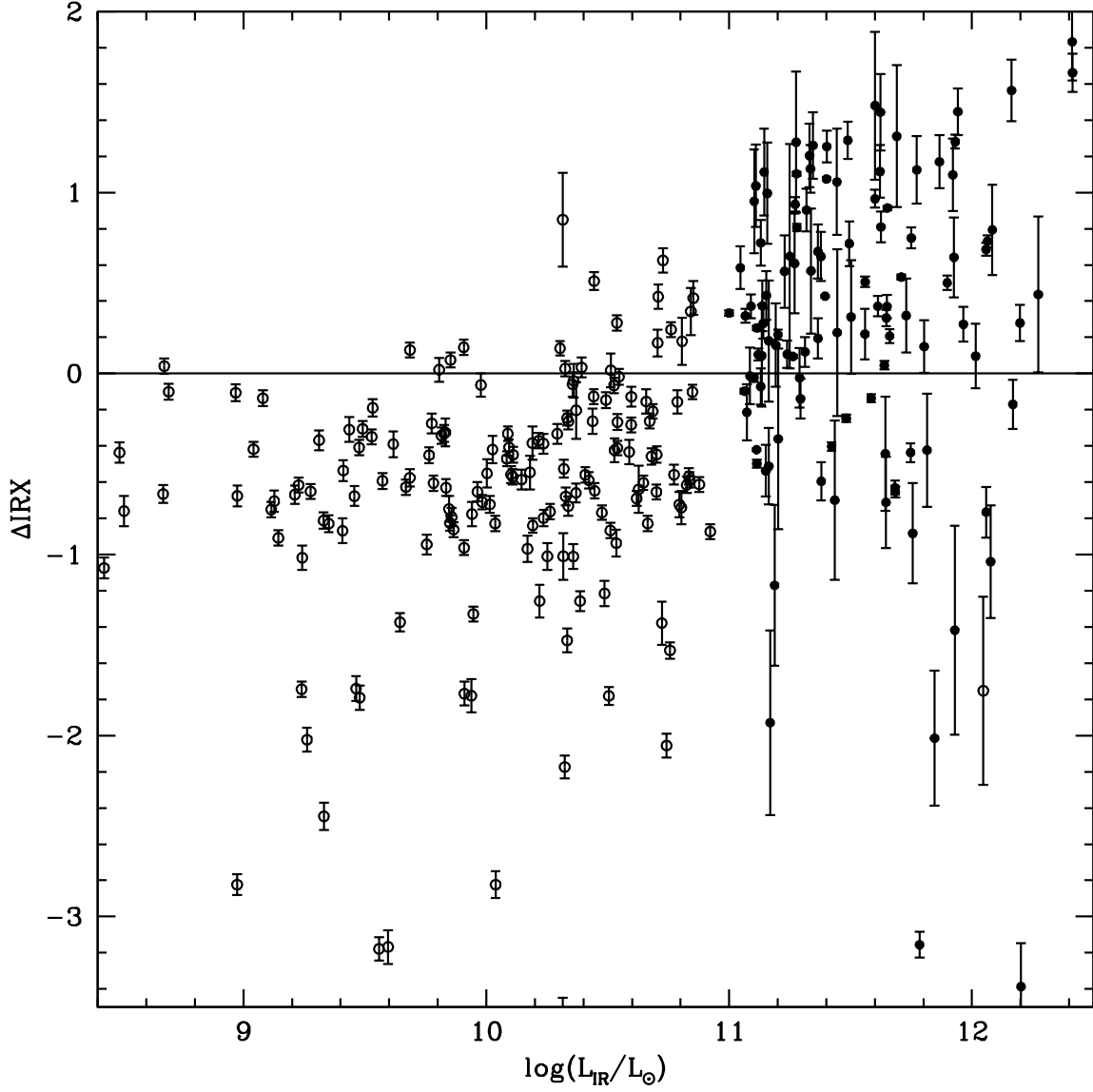


Fig. 8.— ΔIRX vs. L_{IR} . GOALS systems are shown as solid points, while galaxies from GDP are shown as open points. ΔIRX increases with IR luminosity for $L_{\text{IR}} \gtrsim 10^{10} L_{\odot}$.

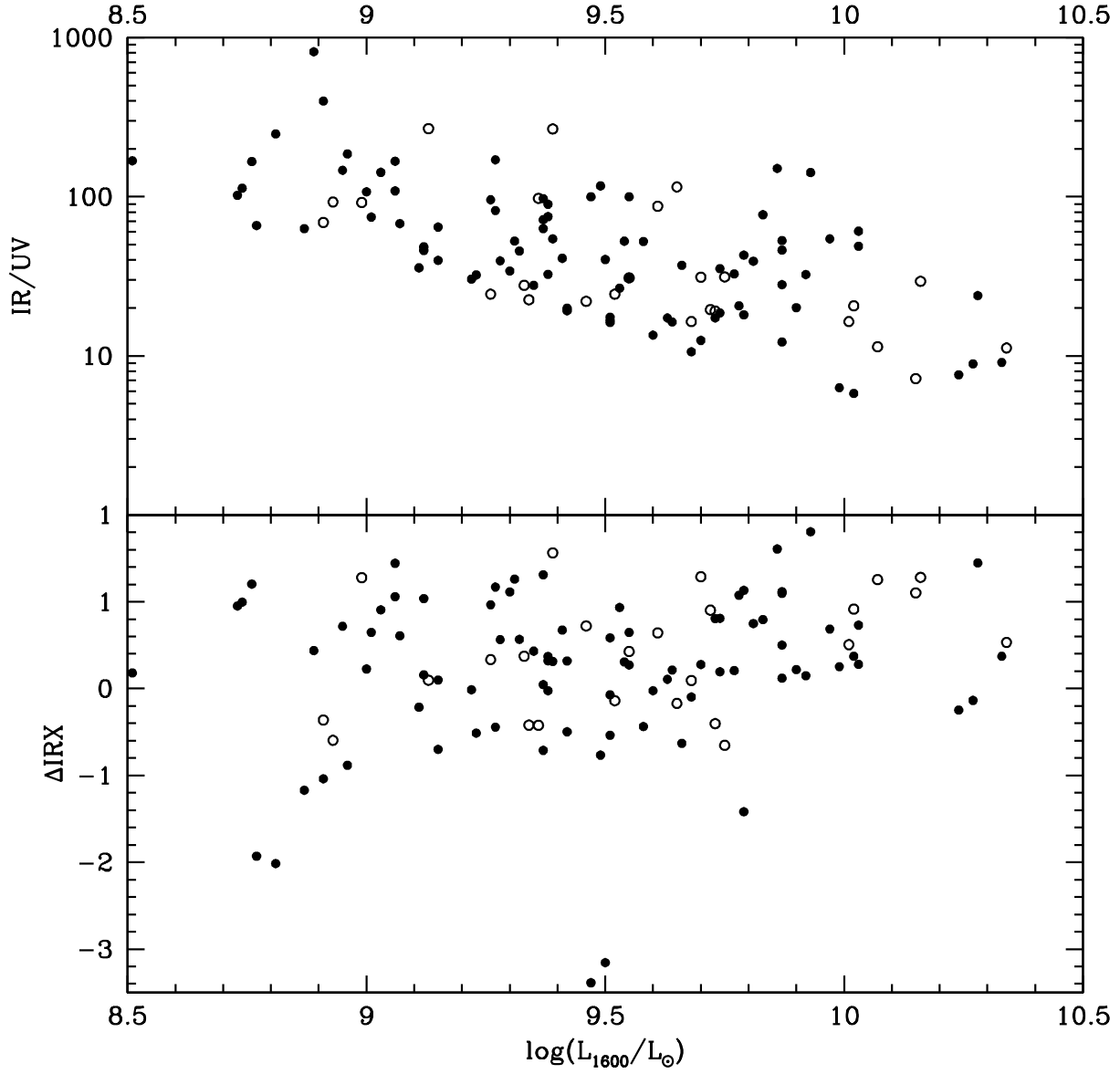


Fig. 9.— Top: The IR/UV ratio plotted against L_{1600} , the luminosity at 1600\AA (interpolated from FUV and NUV). The lower envelope shows the sample selection cutoff of $L_{IR} > 10^{11} L_{\odot}$. Bottom: ΔIRX vs. L_{1600} . No trend is seen; galaxies of high ΔIRX span the full range of UV luminosity. In both panels, galaxies with IRAC colors suggesting a significant AGN contribution are shown as open circles.

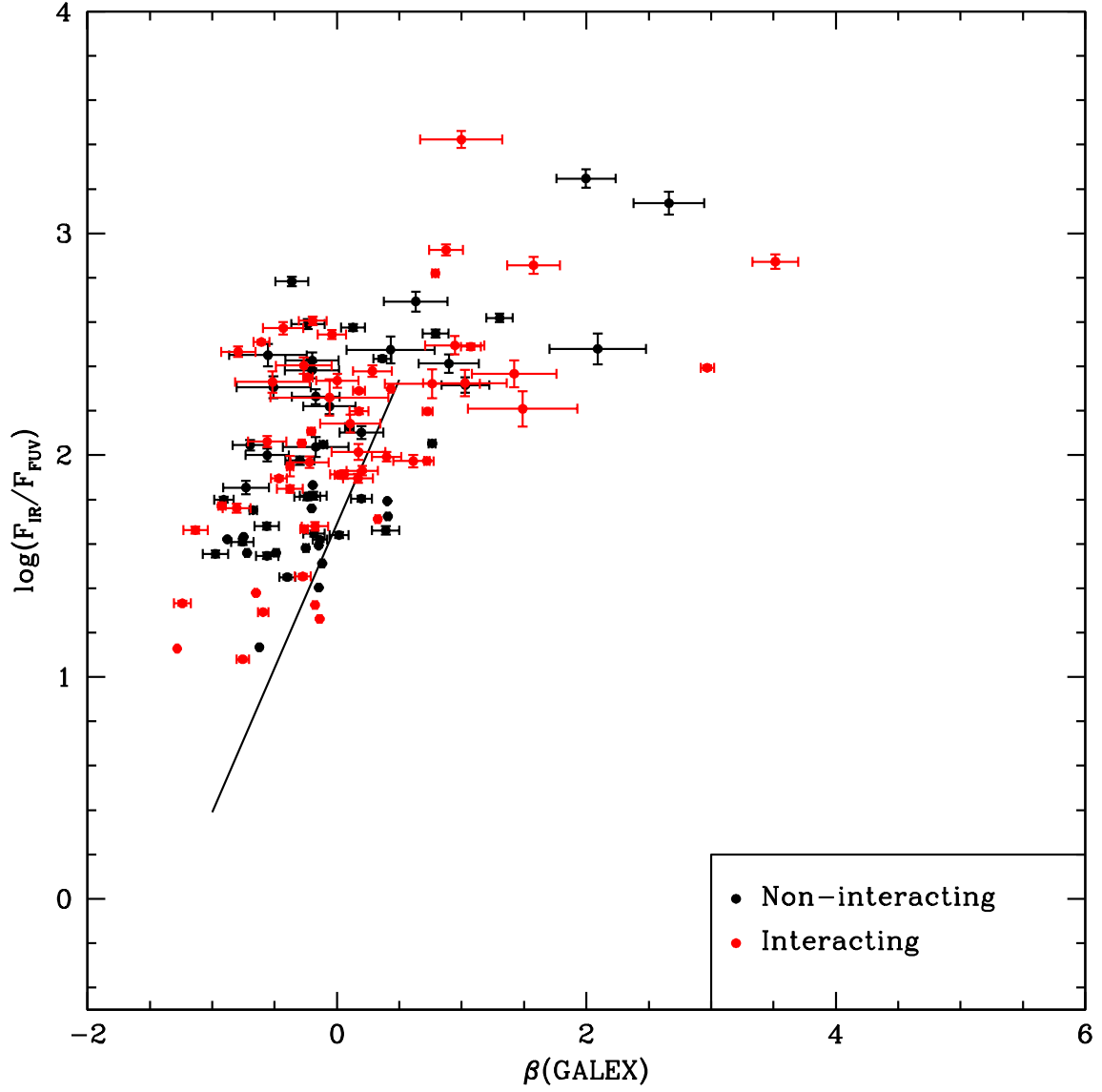


Fig. 10.— IRX- $\beta(\text{GALEX})$ plot comparing interacting (red) and non-interacting (black) LIRG systems. The solid line is the same as in Fig. 1. The interacting and non-interacting populations are consistent with being drawn from the same distribution.